

Evolution of bottom boundary layers on three dimensional topography – Buoyancy adjustment and instabilities

Arjun Jagannathan¹, Kaushik Srinivasan², James C. McWilliams², Jeroen Molemaker², and Andrew Stewart²

¹Indian Institute of Technology Madras

²University of California Los Angeles

December 7, 2022

Abstract

A current along a sloping bottom gives rise to upwelling, or downwelling Ekman transport within the stratified bottom boundary layer (BBL), also known as the bottom Ekman layer. In 1D models of slope currents, geostrophic vertical shear resulting from horizontal buoyancy gradients within the BBL is predicted to eventually bring the bottom stress to zero, leading to a shutdown, or λ arrest λ , of the BBL. Using 3D ROMS simulations, we explore how the dynamics of buoyancy adjustment in a current-ridge encounter problem differs from 1D and 2D temporal spin up problems. We show that in a downwelling BBL, the destruction of the ageostrophic BBL shear, and hence the bottom stress, is accomplished primarily by nonlinear straining effects during the initial topographic counter. As the current advects along the ridge slopes, the BBL deepens and evolves toward thermal wind balance. The onset of negative potential vorticity (NPV) modes of instability and their subsequent dissipation partially offsets the reduction of the BBL dissipation during the ridge-current interaction. On the upwelling side, although the bottom stress weakens substantially during the encounter, the BBL experiences a horizontal inflectional point instability and separates from the slopes before sustained along-slope stress reduction can occurred. In all our solutions, both the upwelling and downwelling BBLs are in a partially arrested state when the current separates from the ridge slope, characterized by a reduced, but non-zero bottom stress on the slopes.

Evolution of bottom boundary layers on three dimensional topography – Buoyancy adjustment and instabilities

Arjun Jagannathan ^{1*}, Kaushik Srinivasan ¹, James C. McWilliams ¹, Jeroen Molemaker ¹,
Andrew L. Stewart ¹

¹Department of Atmospheric and Oceanic Sciences, University of California, Los Angeles, CA 90024, USA

Key Points:

- A complex interplay of buoyancy adjustment, instabilities, and curvature effects influences oceanic bottom boundary layers (BBL) evolution.
- Nonlinear strain effects contribute significantly in weakening the bottom stress during the initial current-ridge encounter.
- The onset of negative potential vorticity (NPV), and barotropic instabilities downstream partially offsets the reduced boundary dissipation.

*Current address, Indian Institute of Technology Madras, Chennai 600036, India

Corresponding author: Arjun Jagannathan, arjunj@iitm.ac.in

Abstract

A current along a sloping bottom gives rise to upwelling, or downwelling Ekman transport within the stratified bottom boundary layer (BBL), also known as the bottom Ekman layer. In 1D models of slope currents, geostrophic vertical shear resulting from horizontal buoyancy gradients within the BBL is predicted to eventually bring the bottom stress to zero, leading to a shut-down, or ‘arrest’, of the BBL. Using 3D ROMS simulations, we explore how the dynamics of buoyancy adjustment in a current-ridge encounter problem differs from 1D and 2D temporal spin up problems. We show that in a downwelling BBL, the destruction of the ageostrophic BBL shear, and hence the bottom stress, is accomplished primarily by nonlinear straining effects during the initial topographic counter. As the current advects along the ridge slopes, the BBL deepens and evolves toward thermal wind balance. The onset of negative potential vorticity (NPV) modes of instability and their subsequent dissipation partially offsets the reduction of the BBL dissipation during the ridge-current interaction. On the upwelling side, although the bottom stress weakens substantially during the encounter, the BBL experiences a horizontal inflectional point instability and separates from the slopes before sustained along-slope stress reduction can occur. In all our solutions, both the upwelling and downwelling BBLs are in a partially arrested state when the current separates from the ridge slope, characterized by a reduced, but non-zero bottom stress on the slopes.

Plain Language Summary

At the ocean surface, winds pump mechanical energy into the ocean at an average rate of between 0.8 TW and 1 TW. This wind-input occurs mainly at large, so-called synoptic scales spanning thousands of kilometers. Absent dissipative pathways, this steady energy input would cause uncontrolled spinup of the ocean gyres. For decades it has been assumed that friction at the seabed has an important role in the eventual turbulent dissipation of the ocean kinetic energy. In the 1990s, theoretical models suggested that turbulence could be wholly suppressed on sloping bottom bathymetry due to the rearrangement of density surfaces within the bottom boundary layer — a mechanism called buoyancy adjustment. Here we revisit this problem using modern 3D simulations of currents encountering a ridge. We find that although the bottom stress can be markedly reduced on topographic slopes, the mechanism through which it occurs is quite different than that in simplified 1D and 2D models. Flow ‘deformation’, or straining effects during the topographic encounter play a more important role in weakening the bottom stress than buoyancy adjustment. Furthermore, geometric effects like curvature, and

45 flow instabilities can partially offset the reduction in dissipation caused by suppression of bot-
46 tom boundary layer turbulence.

47 **1 Introduction**

48 When a bottom boundary layer (BBL) develops over sloping bathymetry, buoyancy ad-
49 vection in the cross-slope direction produces horizontal buoyancy gradients within the BBL,
50 and hence a geostrophic vertical shear through the thermal wind balance. This process, known
51 as buoyancy adjustment (or Ekman adjustment), acts to oppose the ageostrophic boundary layer
52 shear, thereby weakening the bottom stress on the slopes. In simplified models of slope cur-
53 rents (MacCready & Rhines, 1991; Garrett et al., 1993), a steady state is eventually reached
54 in which the bottom stress collapses, bringing the cross slope Ekman transport to zero — a
55 state referred to in the literature as ‘Ekman arrest’. These predictions have been validated in
56 1D numerical models (Brink & Lentz, 2010a), but questions remain about their relevance to
57 the real ocean.

58 Ekman pumping/suction resulting from the horizontal divergence of the Ekman trans-
59 port is thought to be the primary mechanism behind the spin-down of interior flows in the ocean
60 (Garrett et al., 1993). The drag exerted at the seafloor is also estimated to be an important source
61 of energy dissipation (Wunsch & Ferrari, 2004; Sen et al., 2008). Reduced bottom stress and
62 weakening turbulence in sloping BBLs could therefore have profound implications for our un-
63 derstanding of the global oceanic circulation and energy budget (Ruan, Wenegrat, & Gula, 2021).
64 Umlauf et al. (2015) developed a theoretical framework to understand the energetic pathways
65 during the process of Ekman arrest in a 1D BBL, which they then validated using simulations
66 with a second order turbulence closure model. An interesting finding was that buoyancy ad-
67 justment in a BBL is very effective at converting the kinetic energy of the along-slope flow
68 to available potential energy. In particular, for a downwelling (upwelling) BBL, the amount
69 of energy stored as available potential energy after Ekman arrest (defined by the authors as
70 bottom stress reducing below a threshold value) is as large as 40% (70%) of the energy lost
71 to dissipation during the active adjustment process. Crucially, this means that during relaxation
72 from an arrested state, this available potential energy stored in the BBL can be converted to
73 turbulent kinetic energy and eventually dissipated. The implication is that the observation of
74 a partially arrested BBL in some region along the seafloor does not preclude the same region
75 from being a hotspot of dissipation in a different observational window.

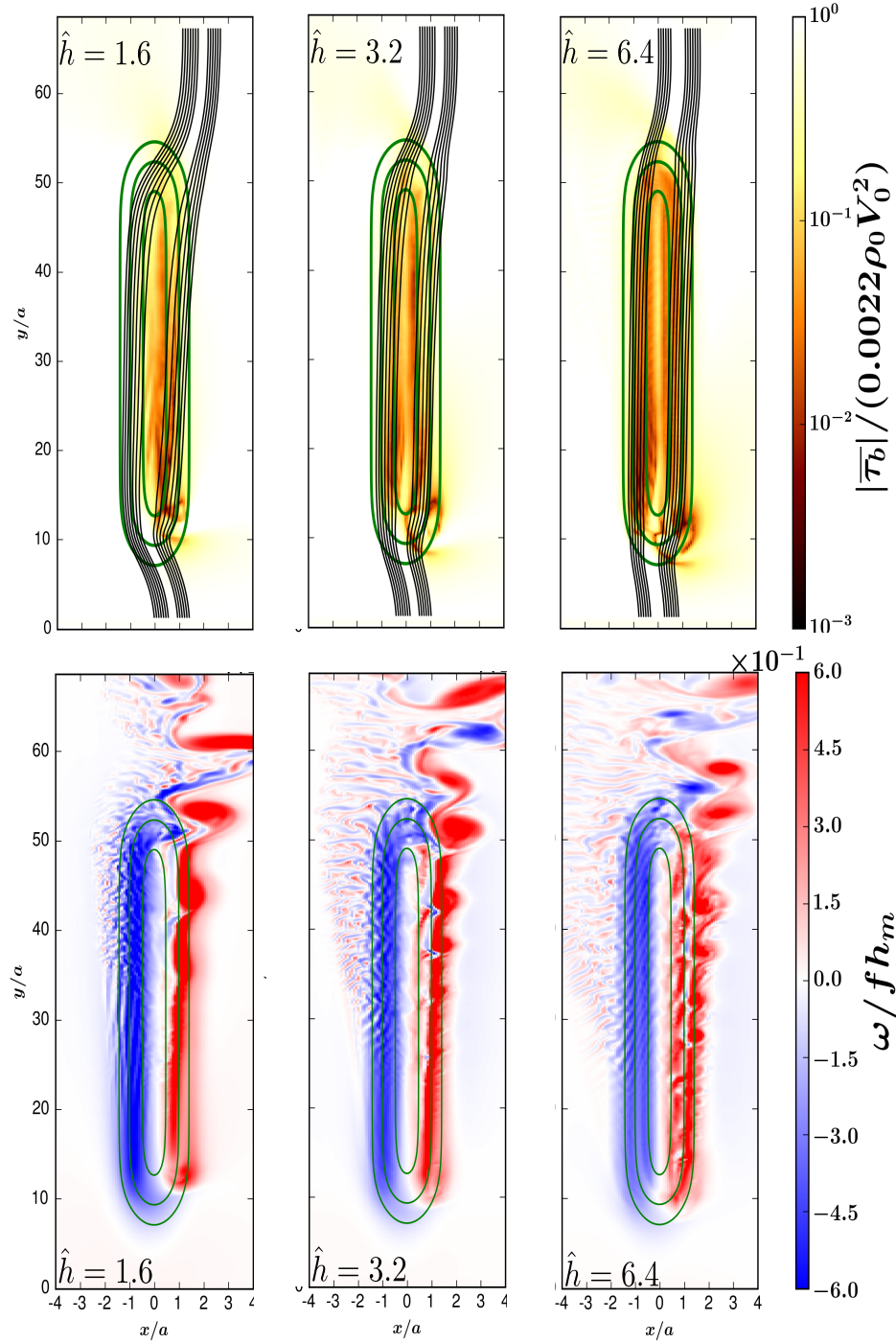


Figure 1. (Adapted from Figs. 1, 4 of Jagannathan et al., 2021, © American Meteorological Society. Used with permission.) Encounter of a barotropic inflow with an elongated racetrack shaped ridge. Green lines are bathymetric contours at $z = 0.14h_m$, $z = 0.37h_m$ and $z = 0.9h_m$. The inflow is from south to north. (Top) Normalized, time-averaged boundary stress $|\overline{\tau_b}|/(C_d^* \rho_0 V_0^2)$, with a value $C_d^* = 0.0022$ (Sen et al., 2008; Arbic et al., 2009), along with selected barotropic streamlines (in black). Dark colors indicate stress reduction. Note that the colormap is saturated at 10^{-1} . (Bottom) Instantaneous snapshots of normalized depth integrated vertical vorticity. Small scale NPV instabilities are visible as banded patterns of vorticity on the anticyclonic side. Values of the parameter \hat{h} are indicated inside each panel. Observe that the instability is triggered further and further upstream for increasing \hat{h} (Note: The vortices appear distorted as the figure is not to scale)

76 Some of the best available observational evidence for reduced bottom stress, or ‘partial
77 arrest ’ over topography is described in Lentz and Trowbridge (2001). These authors analyzed
78 moored current observations in the Northern California mid-shelf during the fall/winter period
79 in 5 different years between 1981 and 1991. Among their findings is that isopycnals slope down-
80 ward near the bottom and that the flow is close to a state of thermal wind balance through-
81 out the water column. The near-bottom along-shelf currents, and hence bottom stress are thus
82 found to be substantially weakened.

83 Complete Ekman arrest nevertheless remains elusive in oceanic observations of the BBL
84 (Armi & Millard Jr, 1976; Armi, 1978; Armi & D’Asaro, 1980). Some recent studies provide
85 clues on why this may be the case. Using LES simulations with doubly periodic boundary con-
86 ditions in the cross- and along-slope directions, Ruan et al. (2019) showed that the BBL al-
87 ways relaminarizes before Ekman arrest can be achieved. The relaminarization, or turbulence
88 collapse, in their solutions is clearly evident in Hovmöller diagrams that show negligible TKE
89 within the BBL at later times (Fig. 12 in Ruan et al. (2019) and Fig. 6 in Ruan, Thompson,
90 and Taylor (2021)). Once the BBL relaminarizes, subsequent evolution toward an arrested state
91 can only proceed via non-turbulent molecular mixing, which is a relatively slow process. Wenegrat
92 and Thomas (2020) further demonstrate how the arrest process can be delayed due to the on-
93 set of negative potential vorticity (NPV) instabilities.

94 To date, most numerical studies on Ekman arrest have focussed on the temporal adjust-
95 ment problem in 1D (e.g. Brink & Lentz, 2010a, 2010b) and more recently, periodic 2D do-
96 mains (e.g. Ruan et al., 2019; Wenegrat & Thomas, 2020). In the real ocean, however, buoy-
97 ancy adjustment on continental shelf slopes or isolated islands, evolves spatially in the along-
98 slope direction. Moreover it does not occur in isolation and is often complicated by other pro-
99 cesses like vorticity generation, waves, and three dimensional instabilities. In the present work
100 we analyze a set of idealized numerical simulations to examine how buoyancy adjustment, and
101 consequently the bottom stress, evolve in a 3D slope-current encounter. This is a follow-up
102 study to an earlier paper Jagannathan et al. (2021) in which we investigated the mechanism
103 of vertical vorticity generation during the interaction of a boundary current with a topographic
104 ridge. The key finding in that paper was that much of the irreversible vertical vorticity is gen-
105 erated during the early encounter of the flow with the ridge, through the so-called bottom stress
106 divergence torque (BSDT). The simulations analyzed here are those described in Jagannathan
107 et al. (2021) along with an additional set of simulations in which we vary the ridge curvature
108 in the along-slope direction.

109 Fig. 1 depicts the essential dynamics involved along with the basic flow and ridge con-
 110 figuration. The elongated ridge is well-suited to explore buoyancy adjustment amidst the full
 111 complexity of 3D motions including ageostrophic NPV instabilities (Wang et al., 2014), vor-
 112 ticity generation, flow separation and secondary circulations. In the following sections we de-
 113 scribe the numerical model setup, analyze the buoyancy adjustment and BBL evolution in our
 114 solutions, along with its energetics, and discuss these results in the context of 1D and 2D the-
 115 ories of Ekman arrest on a slope.

116 2 Numerical setup

117 2.1 Basic model configuration

118 The simulations are performed using the Regional Ocean Modelling System (ROMS)
 119 (Shchepetkin & McWilliams, 2003), a terrain following model that solves the Boussinesq prim-
 120 itive equations under the hydrostatic approximation. The flow configuration is identical to that
 121 described in Jagannathan et al. (2021). For the sake of brevity, we confine our description here
 122 to the most essential aspects of the setup and refer the reader to Jagannathan et al. (2021) for
 123 further details.

124 A uniform barotropic inflow with speed

$$V_0(x, y = 0, z) = 0.105 \text{ ms}^{-1} \quad (1)$$

125 and approximately uniform stratification N is incident on a ridge of height h_m . We consider
 126 two different ridge configurations. The first is the ridge considered in (Jagannathan et al., 2021).
 127 This ridge is elongated in the y direction, with bathymetry contours resembling a racetrack (Fig.
 128 1),

$$h = h_m e^{-x^2/a^2} \left[\frac{1 + \tanh\left(\frac{y-y_1}{\sigma_y}\right)}{2} \right] \left[\frac{1 + \tanh\left(\frac{y_2-y}{\sigma_y}\right)}{2} \right]. \quad (2)$$

129 The second is an elliptical ridge with varying aspect ratio $\beta = b/a$, where b is the half-length,

$$h = h_m e^{-\left(\frac{x^2}{a^2} + \frac{y^2}{b^2}\right)}. \quad (3)$$

130 The ridge is centered in a computational domain that is 240 km long and 90 km wide.
 131 A zero-gradient condition is imposed on the barotropic (vertically-averaged) component of ve-
 132 locity and potential temperature at the lateral and outflow boundaries, while the Orlanski ra-
 133 diation condition (Orlanski, 1976) is specified for the baroclinic component. In all the sim-
 134 ulations, the water depth $H = 1000$ m, the ridge height $h_m = 400$ m and its half-width $a =$

135 3.5 km. The length of the elongated ridge is fixed at $b = y_2 - y_1 = 144$ km and the extent
 136 of the initial adjustment region over which the ridge elevation increases to h_m is given by $\sigma_y =$
 137 12 km.

138 2.2 Buoyancy adjustment on finite ridges with varying topographic slope

139 The critical dimensionless parameter (Srinivasan et al., 2019; Jagannathan et al., 2021)
 140 is the non-dimensional height

$$\hat{h} = \frac{Nh_m}{fa}, \quad (4)$$

141 where f is the Coriolis frequency. In the Ekman arrest literature where the slope $\tan \theta$ is typ-
 142 ically chosen to be constant, the slope Burger number is defined as

$$Bu = N \tan \theta / f \approx N \theta / f, \quad (5)$$

143 for $\theta \ll 1$ (Brink & Lentz, 2010a; Wenegrat & Thomas, 2020). The parameter \hat{h} in our sim-
 144 ulations may thus be regarded as analogous to a slope Burger number, with $\theta = h_m/a$ being
 145 an average measure of the varying topographic slope.

146 Compared to earlier 1D and 2D solutions of buoyancy adjustment on a slope, our setup
 147 has two significant novelties. One is the non-constant slope and the other is the three dimen-
 148 sionality which introduces the possibility of flow separation, topographic waves and secondary
 149 horizontal circulations. To more precisely isolate the 3D effects, one may be tempted to sep-
 150 arately consider the non-constant slope problem in 2D before attacking the 3D problem. How-
 151 ever in practice we found that it is challenging to maintain a steady barotropic forcing in ROMS
 152 for the 2D slope current configuration. To see why this is the case, recall that the flow is ini-
 153 tialized with a constant sea-surface gradient that geostrophically balances a barotropic inflow
 154 (Jagannathan et al., 2021). In 3D, specifying the sea surface height at the inflow boundary *and*
 155 the lateral boundaries is found to be sufficient to maintain a steady barotropic velocity every-
 156 where downstream. However in the 2D configuration, once the flow is initialized, the only way
 157 to hold the barotropic inflow fixed as the flow evolves is by nudging either the sea surface height
 158 or the barotropic velocity itself. Both of these represent strong external forcing of the flow and
 159 introduce artefacts to the solution. For this reason, we directly consider the more realistic 3D
 160 problem without imposing any artificial constraints on the evolution of the along-slope flow.

161 The long straight section of the elongated ridge helps to isolate the buoyancy adjustment
 162 process and facilitates comparison with 1D and 2D model predictions. We focus here on the

163 solutions with $\hat{h} = 1.6, 3.2, 6.4$ and 12.8 . As described in Jagannathan et al. (2021), \hat{h} in these
 164 simulations is varied by changing the stratification N while keeping the other parameters un-
 165 changed. The Coriolis frequency f is fixed at a value of $7 \times 10^{-5} s^{-1}$ and N ranges from $\times 10^{-3} s^{-1}$
 166 in the $\hat{h} = 1.6$ run to $8 \times 10^{-3} s^{-1}$ in the $\hat{h} = 12.8$ run.. For the elliptical ridge, \hat{h} is fixed at
 167 3.2 and the semi-major length b is varied between 3.5 km and 56 km, so that the ellipse as-
 168 pect ratio β spans values ranging from 1 to 16 . Note that outside of the tropics, values of $\hat{h} >$
 169 2 are rare in the ocean. However the local value of \hat{h} , defined as $N_l \theta_l / f$, where N_l and s_l are
 170 respectively the local value of the stratification and slope, can often be quite large, especially
 171 in locations where the thermocline intersects topography. For example, the slope angle in the
 172 Florida straits is as high as 3° in the stretch prior to when the Gulf Stream separates (Gula
 173 et al., 2015). Using a mid-latitude value of $f = 7 \times 10^{-5} s^{-1}$ and typical thermocline strati-
 174 fication $N \approx 10^{-2} s^{-1}$ then gives $\hat{h} \approx 7.5$. Furthermore, as demonstrated in Srinivasan et al.
 175 (2019) and Perfect et al. (2018), when $\hat{h} > 1$ the flow outside the BBL is largely on horizon-
 176 tal planes, meaning that the local \hat{h} value effectively controls the cross-slope BBL dynamics.
 177 Therefore idealized simulations with large \hat{h} can yield useful insight into the dynamics of buoy-
 178 ancy adjustment on realistic continental slopes.

179 **2.3 Bottom stress parameterization and grid resolution**

180 The bottom stress in ROMS is parameterized using the quadratic drag law

$$\boldsymbol{\tau}_b = \rho_0 C_d \mathbf{u}_b \|\mathbf{u}_b\|. \quad (6)$$

181 where ρ_0 is the constant reference density, \mathbf{u}_b is the velocity in the bottommost σ layer and
 182 C_d is the drag constant

$$C_d = [\kappa / \log(\Delta z_b / z_{ob})]^2. \quad (7)$$

183 $\kappa = 0.4$ in Eq. (7) is the Von-Karman constant, Δz_b is the thickness of the bottommost σ -layer
 184 and z_{ob} is the roughness length which we set to 1 cm. Substituting these parameters in Eq. (7),
 185 along with the observed range of values of Δz_b in our runs of 0.9 - 1.1 m, we find that C_d ranges
 186 from 0.0076 over the flat bottom to 0.0083 over the ridge crest.

187 Previous experience with ROMS suggests that NPV phenomena such as forced symmet-
 188 ric instability (Wenegrat et al., 2018) are captured to some degree even in moderately coarse
 189 hydrostatic simulations (500 m in Wenegrat et al. (2018)). In all our simulations we employ
 190 a grid spacing of 300 m in the horizontal and 110 σ - levels, to resolve submesoscale and BBL
 191 processes. With vertical grid stretching the near bottom vertical resolution is as fine as 0.9 m

192 over the ridge crest and 1.1 m over the flat bottom. Vertical mixing in the BBL is parameter-
 193 ized using KPP (Large et al., 1994; McWilliams et al., 2009). The model also implicitly con-
 194 tains horizontal hyperviscosity and hyperdiffusivity via the third-order upwind-biased scheme
 195 (Shchepetkin & McWilliams, 2003, 2005). Time-averages, where shown, are obtained by av-
 196 eraging the relevant quantities over 50 inertial periods.

197 **3 Review of 1D and 2D model predictions**

198 In the northern hemisphere, the Ekman transport in a bottom Ekman layer is to the left
 199 of the interior geostrophic current. On a slope where the current is prograde, i.e. in the direc-
 200 tion of a coastal Kelvin wave, the cross-slope transport results in downwelling of lighter wa-
 201 ter underneath heavier water, leading to a statically unstable state. Convective mixing then pro-
 202 duces a mixed layer which continues to expand in thickness with time (Trowbridge & Lentz,
 203 1991; MacCready & Rhines, 1991). As the BBL thickens, horizontal buoyancy gradients in-
 204 tensify and the bottom stress weakens due to the thermal wind shear. In classical 1D models
 205 of slope currents, the BBL continues to deepen until complete Ekman arrest occurs (Garrett
 206 et al., 1993). In an upwelling Ekman layer, thermal wind shear similarly acts to reduce the bot-
 207 tom stress. The main difference with respect to the downwelling side is that the upslope ad-
 208 vection of buoyancy makes the BBL increasingly stable, and as a result, thinner than on a flat
 209 bottom. All the theoretical predictions reviewed in this section assume a constant value of the
 210 slope so that \hat{h} below connotes a slope Burger number.

211 Assuming that in the steady state, the BBL is perfectly well-mixed, Trowbridge and Lentz
 212 (1991) derive an estimate for its thickness

$$H_a^{DW} = \frac{V_0}{N\hat{h}}, \quad (8)$$

213 where the superscript denotes ‘downwelling’. However the same authors note that the BBL
 214 formed through convective mixing of a downwelling Ekman flow typically tends to be weakly
 215 stratified rather than perfectly well-mixed. Brink and Lentz (2010a) derive an arrest time scale
 216 for such a weakly stratified BBL assuming a constant gradient Richardson number,

$$T_a^{DW} = \frac{V_0^2(1 + \hat{h}^2)\Pi(\hat{h})}{2u_0^{*2}N\hat{h}^3}, \quad (9)$$

217 where u_0^{*2} is the flat-bottom stress in the absence of buoyancy arrest,

$$\Pi(\hat{h}) = \frac{1 + \sqrt{1 + 4Ri_c\hat{h}^2}}{2}, \quad (10)$$

218 and Ri_c is the critical gradient Richardson number, averaged over an inertial period.

219 2D simulations (Wenegrat & Thomas, 2020) show that the destruction of the BBL strat-
 220 ification through convective mixing is accompanied by a negative flux of potential vorticity
 221 (PV) through the bottom which drives the PV below 0 in the BBL. Here the PV is defined as

$$q = \mathbf{\Omega}_a \cdot \nabla b \quad (11)$$

222 where $b = -g\rho/\rho_0$ is the buoyancy and $\mathbf{\Omega}_a = \hat{\mathbf{k}} + \nabla \times \mathbf{u}$ is the three-dimensional absolute
 223 vorticity.

224 The $q < 0$ state is susceptible to NPV instability modes, which then return the flow to
 225 marginal stability. Wenegrat and Thomas (2020) further demonstrate that the onset of insta-
 226 bility delays, but does not stop the progression to an arrested state. Their modified arrest time
 227 scale is given by

$$T_a^{NPV} = \frac{V_0^2(1 + \hat{h}^2)^2}{2u_0^{*2}N\hat{h}^3}. \quad (12)$$

228 The extra factor $(1 + \hat{h}^2)$ in Eq. (12) comes from substituting $Ri_c = 1 + \hat{h}^2$ in Eq. (10), which
 229 is the condition of marginal stability with $q = 0$ (Allen & Newberger, 1996) . The correspond-
 230 ing expression for the arrest height is

$$H_a^{NPV} = \frac{V_0(1 + \hat{h}^2)}{N\hat{h}}. \quad (13)$$

231 Thus both the arrest time and arrest height are amplified by a factor of $(1 + \hat{h}^2)$ relative to 1D
 232 models in which NPV instabilities are absent. Note that the modification in the arrest height
 233 prediction follows directly from the requirement that $q = 0$ in the BBL.

234 In the upwelling regime, the upslope advection of dense water tends to stabilize the BBL,
 235 making it shallower relative to the downwelling. The numerical experiments of Brink and Lentz
 236 (2010a) show two different end states, depending on the value of \hat{h} . For $\hat{h} > 1$, their solutions
 237 produce a uniformly stratified BBL connecting smoothly to the stratified interior. The BBL
 238 height corresponding to arrest is

$$H_a^{UW} = \frac{V_0}{N\hat{h}}\gamma(\hat{h}), \quad (14)$$

239 where the superscript denotes ‘upwelling’ and $\gamma(\hat{h})$ is given by the functional form

$$\gamma(\hat{h}) = \frac{-1 + \sqrt{1 + 4Ri^{UW}\hat{h}^2}}{2}. \quad (15)$$

240 Brink and Lentz (2010a) further find that $Ri^{UW} = 0.4$ produces a satisfactory fit to their nu-
 241 merical experiments, using either a Mellor-Yamada 2.0 closure or $k - \varepsilon$ model. The correspond-
 242 ing arrest time scale for the upwelling favorable regime is then obtained as

$$T_a^{UW} = \frac{V_0^2(1 + \hat{h}^2)\gamma(\hat{h})}{2u_0^{*2}N\hat{h}^3}. \quad (16)$$

243 On the other hand, when $\hat{h} < 1$, the vertical structure is characterized by a weakly strat-
 244 ified BBL, capped by a strongly stratified pycnocline (Brink & Lentz, 2010a). Buoyancy ad-
 245 justment times are much longer than for $\hat{h} > 1$. In the limit $\hat{h} \ll 1$, the BBL characteristics
 246 approach those of a flat bottom Ekman layer. Interestingly, in their recent LES study, Ruan,
 247 Thompson, and Taylor (2021) note that capped BBLs are not observed. The authors attribute
 248 this to relaminarization of the BBL, which does not occur in simpler turbulence closures. For
 249 more details on the capped BBL we refer the reader to Brink and Lentz (2010a).

250 In one and two dimensional models of slope currents, buoyancy adjustment is a defin-
 251 ing aspect of the solutions in both the $\hat{h} > 1$ and $\hat{h} < 1$ regimes. The only difference is the
 252 considerably longer adjustment time when $\hat{h} < 1$. This can be seen by inspecting Eqs. (9) and
 253 (12) where in the limit $\hat{h} \ll 1$, T_a^{NPV} varies as \hat{h}^3 and T_a^{UW} as $1/\hat{h}$. By contrast, in the case
 254 of an isolated 3D ridge, the $\hat{h} < 1$ regime is quasi-geostrophic (QG) (Schär & Davies, 1988),
 255 with strong cross-isobath flow and vortex stretching effects dominating the dynamics (Srinivasan
 256 et al., 2019; Hogg, 1973; Schär & Davies, 1988). For this reason, we do not consider this regime
 257 here. Focusing on the $\hat{h} > 1$ regime, we will see that the evolution toward Ekman arrest in
 258 a topographic encounter problem has important differences from the lower dimensional tem-
 259 poral spin up problems. In particular, nonlinear straining plays an important role, both in weak-
 260 ening the ageostrophic BBL shear during the initial encounter with the ridge, as well as the
 261 subsequent evolution of the BBL towards thermal wind balance.

262 **4 Results**

263 **4.1 Bottom Stress Evolution on the Slopes**

264 We define the anticyclonic (cyclonic) side of the ridge as the side where uphill is to the
 265 right (left) of the incident flow. Note that, in our flow configuration (Fig. 1) with the Corio-
 266 lis frequency $f > 0$, the bottom Ekman layer is downwelling-favorable on the anticyclonic side
 267 and upwelling-favorable on the cyclonic side. In the discussion that follows, the BBL height
 268 on the cyclonic side refers to the region of active turbulence where shear driven entrainment
 269 and mixing are occurring. This is also the quantity explicitly computed in ROMS using the KPP
 270 formulation McWilliams et al. (2009).

271 On the anticyclonic side, a dynamically consistent definition of the BBL height needs
 272 to account for convective mixing produced by the downwelling Ekman layer as well as sec-
 273 ondary NPV instabilities. Allen and Newberger (1996) show that, in a downwelling Ekman

274 layer, symmetric instability partially restratifies the BBL so that its stratification at marginal
 275 stability ($q=0$) is given by $N^2\hat{h}^2/(1+\hat{h}^2)$. Thus for values of \hat{h} greater than 1, the BBL can
 276 retain substantial stratification. This is well supported by recent observations in the Orkney
 277 passage (Garabato et al., 2019) where the measured \hat{h} is about 1.8 and the BBL stratification
 278 is around two-thirds of the interior value. The solutions analyzed here have \hat{h} values ranging
 279 from 1.6 to 12.8 and as we shall see below, are unstable to NPV instabilities on the anticy-
 280 clonic side.

281 One choice of definition for the BBL height therefore is as the depth over which the ver-
 282 tical buoyancy gradient is less than $N^2\hat{h}^2/(1+\hat{h}^2)$. However our 3D solutions depart from the
 283 2D assumptions implicit in Allen and Newberger (1996) in some important respects: first, the
 284 stratification is not constant in the BBL and so the BBL is never uniformly in a state of marginal
 285 stability; second, as we will see later, the instabilities that develop are not pure symmetric modes
 286 but rather hybrid modes that draw energy from both the mean vertical shear *and* horizontal
 287 shear. Thus we simply define the BBL height as the height from the bottom where the strat-
 288 ification first exceeds $\alpha N^2\hat{h}^2/(1+\hat{h}^2)$, where α is some constant slightly larger than 1, here
 289 taken to be 1.1. A 10% variation in α (say $\alpha = 1.2$ rather than 1.1) does not lead to a ma-
 290 terial difference in the computed BBL heights.

291 The incident flow on the flat bottom has a well-mixed, turbulent BBL, capped by a strongly
 292 stratified pycnocline. The characteristics of the flat bottom Ekman layer have been previously
 293 described by other authors (e.g. Taylor & Sarkar, 2008). The upper panel of Fig. 1 shows the
 294 evolution of the bottom stress as this flat bottom Ekman layer encounters the topography. The
 295 stress values have been normalized by $\rho_0 C_d^* V_0^2$, the expected stress on a flat bottom with far-
 296 field velocity V_0 . The value of the drag coefficient C_d^* when this formula is used, is typically
 297 in the range 0.002-0.003 (Sen et al., 2008; Arbic et al., 2009). Note that C_d^* is different from
 298 C_d used to parameterize the bottom stress in ROMS because the latter is multiplied by V_b^2 (V_b
 299 is the velocity in the bottom-most σ -layer) and not V_0^2 to get the bottom stress (see Eq. 7).
 300 Here we find that $C_d^* = 0.0022$ yields a non-dimensional stress around 1 away from the to-
 301 pography and use this value henceforth in our scalings for stress, energy production and dis-
 302 sipation.

303 The sustained weakening of the stress on the slopes is apparent in Fig. 1. To better vi-
 304 sualize its downstream evolution in a slope-averaged sense, we compute the average stress across
 305 the set of barotropic streamlines depicted in Fig. 1, separately on each side of the ridge, and

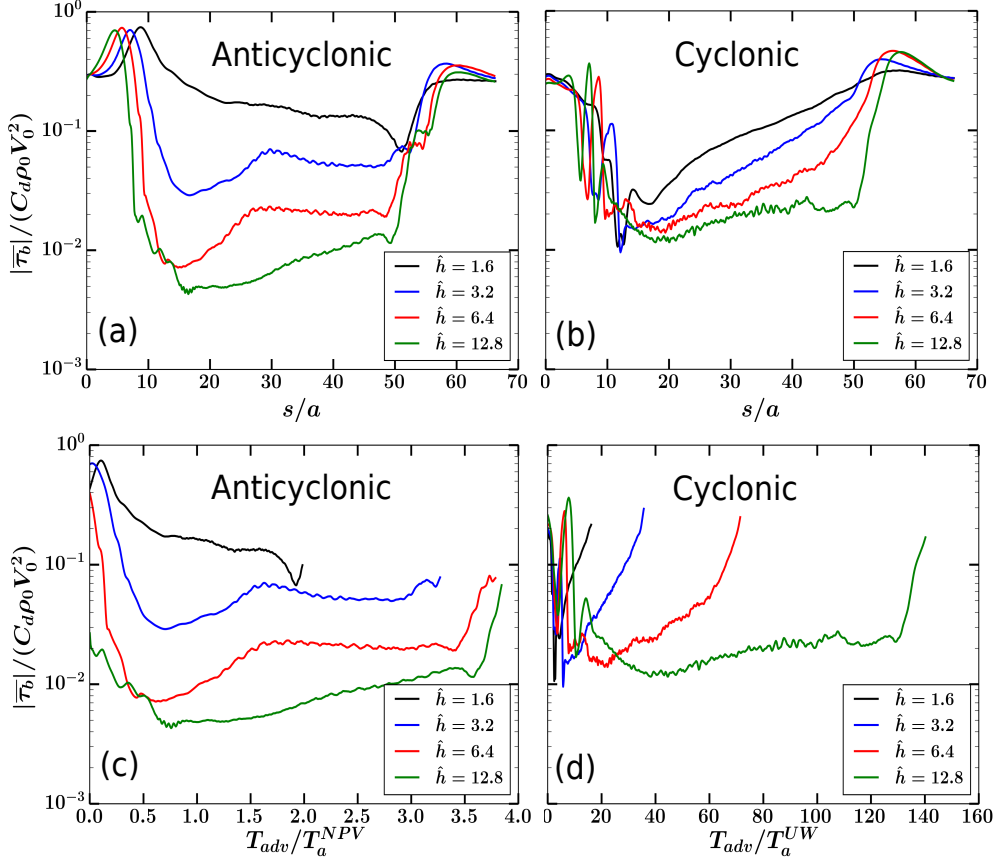


Figure 2. (Top panel) Streamline-averaged evolution of the time-averaged bottom stress shown in Fig. 1 for different values of \hat{h} . (a) Anticyclonic and (b) Cyclonic. (Bottom panel) Evolution of the bottom stress as a function of time. Here $T_{adv} = (s - s_0)/V_0$, where s is the distance travelled along the mean streamline starting from the inflow location $y = 0$, and s_0 is the value of s where the streamline intersects the ridge contour $h(x, y) = h_m \exp(-2)$. Thus T_{adv} is an advective time representative of the transit time of the flow along the ridge slopes. (c) Anticyclonic and (d) Cyclonic. T_a^{NPV} is the time scale for arrest in the presence of NPV instabilities, as derived in Wenegrat and Thomas (2020) (Eq. (12) above) and T_a^{UW} is the Brink and Lentz (2010a) time scale for arrest in the upwelling-favorable regime (Eq. (16) above).

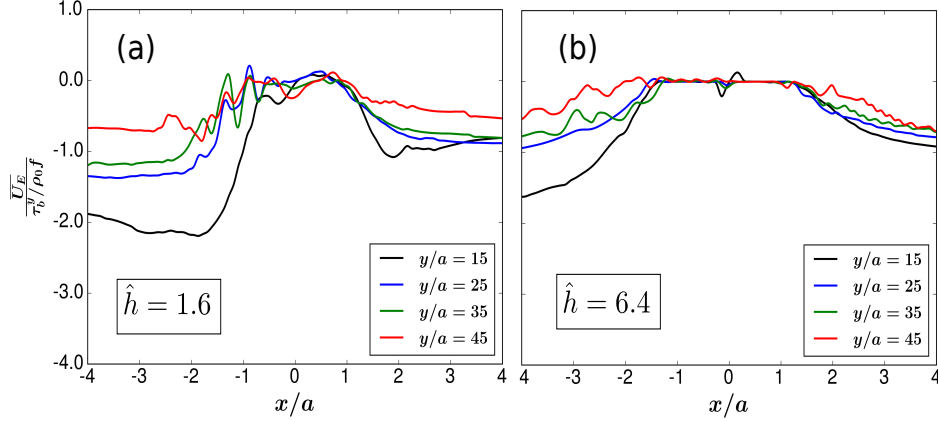


Figure 3. Downstream evolution of the Ekman transport (defined in Eq. (18)) at different downstream locations given by the non-dimensional distance y/a , on and immediately adjacent to the ridge slopes. The values have been normalized by the average Ekman transport over the flat bottom far from the ridge. The \hat{h} values are indicated inside each panel.

306 plot this as a function of along-streamline distance (Figs. 2a,b). The bottom stress starts to de-
 307 crease within a short distance of the well-mixed BBL encountering the ridge. The reduction
 308 is stronger for larger \hat{h} , approaching more than an order of magnitude for $\hat{h} = 3.2$ and higher
 309 (Fig. 2).

310 On the anticyclonic (downwelling) side, the mean streamlines in Fig. 1 show that the
 311 current remains largely attached to the slopes throughout the encounter. As a result, along-stream
 312 fluctuations are muted. By contrast, there are large oscillations on the cyclonic side associ-
 313 ated with the separation and reattachment of eddies during the early encounter (Fig. 1). Af-
 314 ter the early reduction, the stress exhibits a slow increasing tendency downstream.

315 We plot the quasi-temporal evolution of the stress along the barotropic streamlines by
 316 defining an advective time

$$T_{adv} = \frac{s - s_0}{V_0}. \quad (17)$$

317 Here s is the along-streamline distance measured from the inflow location $y = 0$, averaged across
 318 the barotropic streamlines shown in Fig. 1. Note that the averaging is performed separately
 319 on each side of the ridge. s_0 is the value of s where the streamline intersects the ridge con-
 320 tour $h(x, y) = h_m \exp(-2)$. That is, the clock starts ticking where the mean streamline encoun-
 321 ters the ridge and T_{adv} represents the transit time of the flow on the slopes. We use T_a^{NPV} and
 322 T_a^{UW} respectively to scale the advective time T_{adv} on the anticyclonic and cyclonic sides. Note

323 that for all the values of \hat{h} considered here, T_a^{NPV} is significantly longer than T_a^{UW} . Figs. 2c,d
 324 show that the bottom stress slumps by an order of magnitude over $\mathcal{O}(1)$ arrest time scale (T_a^{NPV})
 325 on the anticyclonic side and between $\mathcal{O}(1) - \mathcal{O}(10)$ arrest time scales on the cyclonic side.
 326 Plugging in $V_0 = 0.105 \text{ ms}^{-1}$, $u_0^{*2} = C_d^* V_0^2$, with $C_d^* = 0.0022$ (Sen et al., 2008; Arbic et al.,
 327 2009), and N and \hat{h} for each solution in Eqs. (12) and (16), we find that this corresponds to
 328 $\mathcal{O}(1)$ inertial periods on each side. As we shall show in section 4.2 in our analysis of the ver-
 329 tical shear equation Eq. (19), this initial rapid stress reduction is not due to buoyancy adjust-
 330 ment, but rather a consequence of 3D, nonlinear straining effects when the flow first encoun-
 331 ters the ridge.

332 In response to the diminishing bottom stress, the cross-slope Ekman transport in the BBL

$$U_E = \int_{-H}^{-H+h_{bbl}} u \, dz \quad (18)$$

333 at the upper slopes $|x/a| < 0.5$, approaches zero within a short distance downstream (Fig. 3).
 334 As the current accelerates around the sides, the bottom stress and hence Ekman transport are
 335 enhanced near the lower reaches ($|x/a| > 0.5$) of the ridge. The resulting zonal divergence in
 336 Ekman transport drives Ekman pumping through a secondary upwelling circulation. Vortex stretch-
 337 ing due to Ekman pumping is responsible for intensifying and redistributing the BBL gener-
 338 ated vertical vorticity in the interior (Jagannathan et al., 2021).

339 The flow on the anticyclonic side develops a spatial instability mode which grows to fi-
 340 nite amplitude downstream. This is manifest by the emergence of a banded pattern of small
 341 scale vortices in the lower panel of Fig. 1. The instability begins further and further upstream
 342 for increasing values of \hat{h} . Below we will identify these as belonging to a general class of NPV
 343 instabilities. In the 2D simulations of Wenegrat and Thomas (2020), the flow continues to evolve
 344 toward an arrested state even after the onset of NPV instabilities. From Eq. (12), we would
 345 expect that this 2D arrest time scale T_a^{NPV} is approximately 7.8 inertial periods for the case
 346 $\hat{h} = 1.6$ and 4.3 inertial periods for $\hat{h} = 12.8$. The encounter time in our solutions is around
 347 16 inertial periods on the anticyclonic side (Fig. 2c,d). Thus the 2D expectation of buoyancy
 348 adjustment (e.g. Fig. 16 of Wenegrat and Thomas (2020)) is a monotonic decay of the bot-
 349 tom stress toward zero before the flow separates from the ridge. Yet in Fig. 2, the bottom stress
 350 exhibits a much slower decay than expected for $\hat{h} = 1.6$. For the two intermediate values of
 351 \hat{h} , there is a slight increase after the initial slump, followed by a plateauing of the stress. Like-
 352 wise, the bottom stress on the cyclonic side plunges sharply during the initial encounter but
 353 starts to rebound to higher values over $\mathcal{O}(10)$ arrest time scales. The observations above are

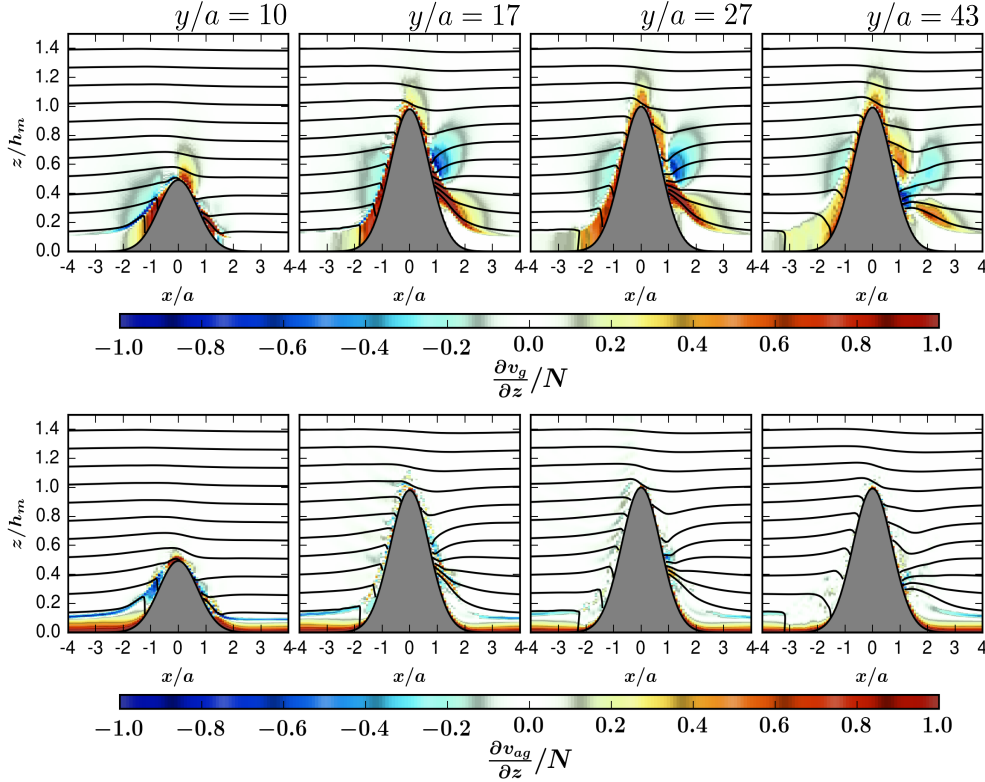


Figure 4. Downstream evolution of the time-averaged vertical shear overlain with the flow isopycnals (top) geostrophic vertical shear $\frac{\partial v_g}{\partial z}/N$ and (bottom) the ageostrophic shear $\frac{\partial v_{ag}}{\partial z}/N$ for the $\hat{h} = 3.2$ solution. The ridge centerline is at $y/a = 30.9$.

354 indicative of the fact that other 3D effects besides buoyancy adjustment exert a strong influ-
 355 ence on bottom stress evolution, and hence turbulent bottom dissipation over topographic ridges.
 356 We will examine these in detail below.

357 4.2 Vertical Shear Balance and the Role of Strain

358 The theoretical state of Ekman arrest is characterized by collapse of the BBL on the slopes
 359 and the establishment of a deep boundary layer in a state of thermal wind balance. To assess
 360 the degree of arrest in our solutions, we decompose the time-averaged vertical shear into its
 361 geostrophic and ageostrophic components. Note that the ageostrophic component here encom-
 362 passes not only shear due to vertical mixing in the BBL but also that due to nonlinear advec-
 363 tive effects such as strain (see Eq. (19) below).

364 Fig. 4 is a representative plot of the component-wise decomposition of the vertical shear
 365 for the case $\hat{h} = 3.2$. Over the flat bottom ($|x/a| > 3$) the shear in the BBL is purely ageostrophic
 366 and is positive except near the pycnocline (see also Taylor & Sarkar, 2008). Shortly after the
 367 current-ridge encounter, at $y/a = 10$, both the geostrophic and ageostrophic components are
 368 significant. Furthermore, on the anticyclonic side, the two components are clearly seen to be
 369 opposite-signed, with the ageostrophic shear being negative. At $y/a = 17$ the ageostrophic com-
 370 ponent of vertical shear has weakened drastically (Fig. 4). It continues to weaken downstream
 371 and by $y/a = 27$, the clear dominance of the geostrophic component signals approach toward
 372 a partially arrested state. Interestingly, the rightmost panel of this figure shows that the geostrophic
 373 shear itself has relatively weakened by $y/a = 43$. As we shall see in section 4.3 this reflects
 374 partial restratification of the BBL following the onset and growth of NPV instabilities.

375 Writing the squared vertical shear as $\|\mathbf{u}_z\|^2 = u_z^2 + v_z^2$, its Lagrangian evolution equa-
 376 tion can be written as (Srinivasan et al., 2021)

$$\frac{1}{2} \frac{D\|\mathbf{u}_z\|^2}{Dt} = - \underbrace{\left[\underbrace{(u_z^2 u_x + v_z^2 v_y)}_{-\Lambda_h} + u_z v_z (u_y + v_x) + \underbrace{\|\mathbf{u}_z\|^2 w_z}_{-\Lambda_v} \right]}_{\Lambda_{nl}} - \underbrace{(b_x u_z + b_y v_z)}_{\Lambda_b} + \underbrace{D(\mathbf{u}_z)}_{\Lambda_{mix}}, \quad (19)$$

377 where $\Lambda_{nl} = \Lambda_h + \Lambda_v$ represents nonlinear horizontal and vertical straining effects, Λ_{mix} is the
 378 shear generation/destruction due to the combined effect of parameterized vertical momentum
 379 mixing and implicit horizontal hyperdiffusion, and Λ_b is the geostrophic production term. We
 380 plot each of the tendency terms on the RHS of Eq. (19) for the three solutions $\hat{h} = 1.6, 3.2$
 381 and 6.4 in Fig. 5. The terms are averaged across-slope and over the local BBL depth on the
 382 anticyclonic side. We do not show an equivalent plot for the cyclonic side as the flow there
 383 separates early, and consequently there is no obvious trend to be discerned from examining
 384 Eq. (19).

385 Before the flow encounters the ridge, turbulent vertical mixing is the primary source of
 386 vertical shear generation in the BBL. This ageostrophic shear is neutralized by nonlinear strain-
 387 ing processes during the early flow adjustment over the topography. Examining Fig. 4 along-
 388 side the middle panel of Fig. 5 one can infer that the negative ageostrophic shear over the an-
 389 ticyclonic slopes at $y/a = 10$ comes largely from nonlinear straining effects Λ_{nl} . Buoyancy
 390 adjustment and strain then combine to bring the flow downstream progressively closer to a state
 391 of geostrophic balance. Downstream of $y/a \approx 12$, note that the total tendency remains slightly
 392 negative. This is consistent with the observed reduction in the intensity of the geostrophic ver-
 393 tical shear at $y/a = 43$ (rightmost panel of Fig. 4).

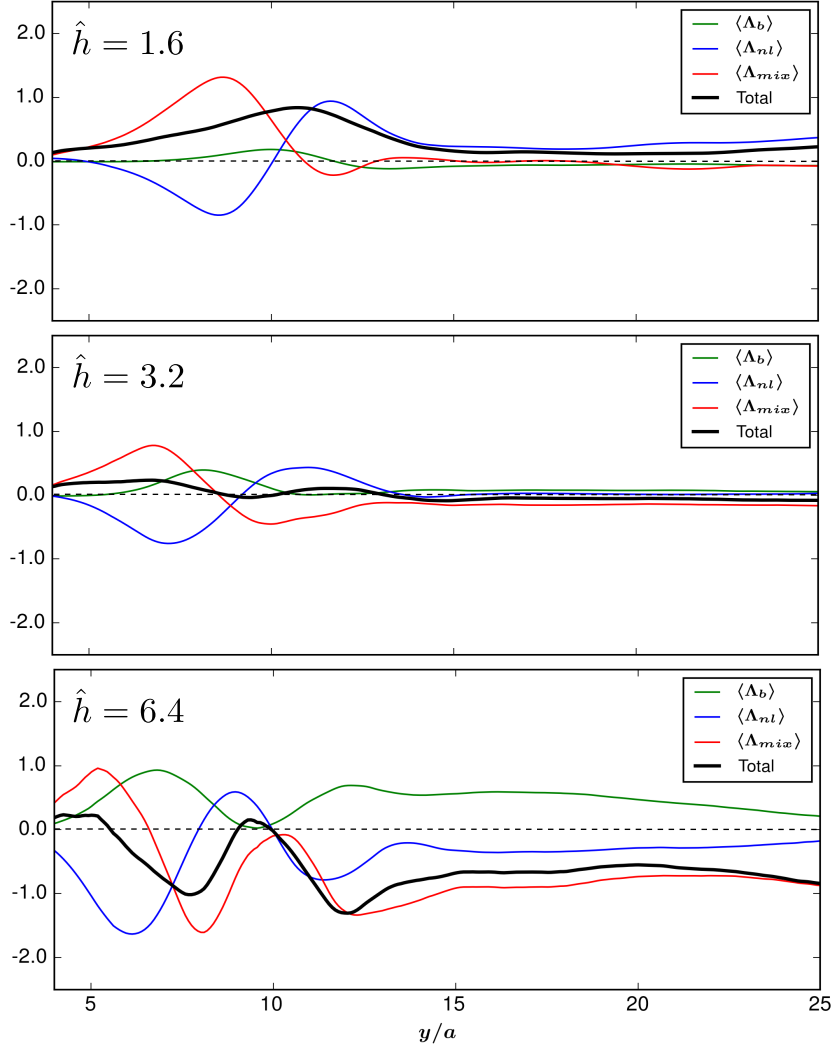


Figure 5. (Anticyclonic) Tendency terms of the time-averaged squared vertical shear equation Eq. (19).

Λ_{nl} represents nonlinear straining effects, Λ_{mix} is the shear generation/destruction due to the combined effect of parameterized vertical momentum mixing and implicit horizontal hyperdiffusion in ROMS, and Λ_b is the geostrophic production term. Each term is normalized by $NV_0^2 h_m^{-2}$ and averaged over the local BBL depth and in the across-slope direction. \hat{h} values are indicated inside each panel. The zero line is shown dashed for clarity.

394 Note that the peaks and troughs of all the tendency terms shift upstream with increas-
 395 ing \hat{h} , reflecting faster adjustment times for higher \hat{h} (Eqs. (9), (12)). A comment on the bot-
 396 tommost panel of Fig. 5 showing the tendency terms for $\hat{h} = 6.4$: interestingly, the combined
 397 effect of λ_{nl} and Λ_{mix} produces two prominent troughs in the total vertical shear tendency. The
 398 exact reason for this pattern is not clear; however the relatively large negative value of the to-
 399 tal tendency downstream of $y/a = 15$ is consistent with the expected strong restratifying ef-
 400 fects in the BBL for high \hat{h} (Allen & Newberger, 1996) which will substantially weaken the
 401 geostrophic vertical shear.

402 Strong nonlinear, 3D straining motions during the initial flow adjustment over the ridge
 403 thus strongly influence the dynamics of buoyancy adjustment on the slopes. In particular, the
 404 strain term neutralizes the ageostrophic BBL shear of the incident flow, and then acts in con-
 405 cert with the geostrophic production term Λ_b to produce a more rapid initial stress reduction
 406 (Fig. 2c,d) than predicted by 1D or 2D models where strain effects are absent. Note that this
 407 is a rather different phenomenological sequence compared to 1D models where buoyancy ad-
 408 justment alone acts to convert ageostrophic shear to geostrophic shear.

409 **4.3 BBL instabilities, energetics and dissipation**

410 The conversion from ageostrophic to geostrophic vertical shear in the BBL is associated
 411 with an expanding region of negative PV. Figs. 6a,b show the evolution of the stratification
 412 and PV over the anticyclonic slope for the $\hat{h} = 3.2$ solution. A well-mixed BBL with $q \approx 0$
 413 encounters the topography. The lower part of the BBL initially develops NPV due to convec-
 414 tive overturning (Fig. 6b). The region of weak stratification deepens and the pycnocline is even-
 415 tually destroyed further downstream (Fig. 6a). As the gesotrophic vertical shear is established,
 416 the NPV layer becomes increasingly deeper.

417 The $q < 0$ state is susceptible to instability, which can be categorized in different ways
 418 depending on the the dominant energy conversion terms (Wang et al., 2014; Thomas et al., 2013).
 419 Fig. 6c shows that the horizontal component $q_h \approx -v_z b_x$ contributes substantially to the neg-
 420 ative PV in the mixed layer, hinting at the possibility of symmetric instability (Thomas et al.,
 421 2013). To gain further insight into the nature of the instability here (visible as bands of insta-
 422 bility on the anticyclonic side in the bottom row of Fig. 1), we compute the production terms
 423 of the eddy kinetic energy (EKE) equation. Energy is transferred from the mean flow to the

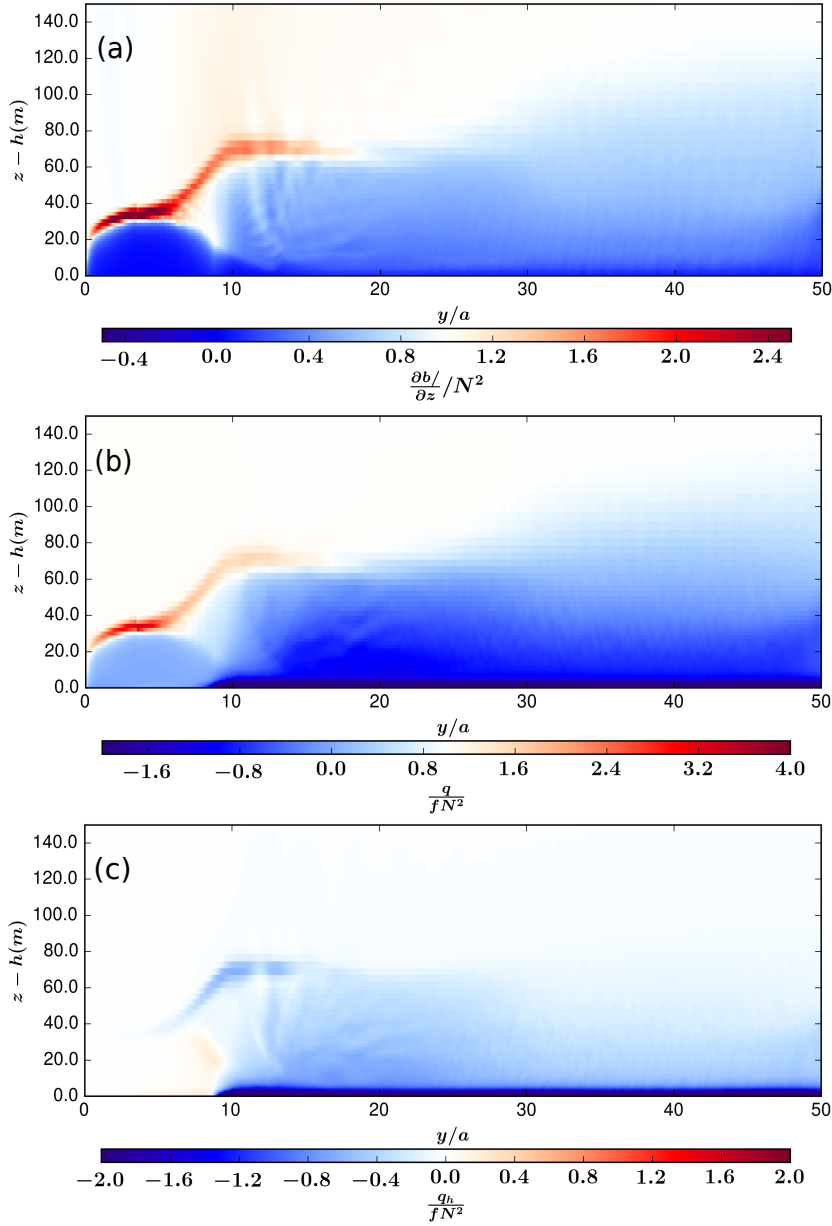


Figure 6. Downstream evolution of the time-averaged vertical buoyancy gradient and PV on the anticyclonic side for the $\hat{h} = 3.2$ solution. Over the ridge, each of the quantities is averaged across the slope and plotted as a function of height from the ridge bottom. On the flat bottom before the encounter, the color contours displayed are for the centerline $x/a = 0$ values. (a) $\partial b / \partial z$ normalized by the background squared Brunt Vaisala frequency N^2 . (b) Normalized potential vorticity q / fN^2 and (c) the horizontal component of potential vorticity q_h / fN^2 .

424 eddies through the vertical and horizontal Reynolds stress work, defined respectively as

$$VRS = -(\overline{u'w'u_z} + \overline{v'w'v_z}), \quad (20)$$

425 and

$$HRS = -(\overline{u'u'u_x} + \overline{u'v'u_y} + \overline{v'v'v_y} + \overline{u'v'v_x}), \quad (21)$$

426 where the overbar $\overline{(\cdot)}$ denotes a time average and primed quantities $(\cdot)'$ are perturbations about
 427 the average. Reversible exchange of available potential energy between the mean and eddy fields
 428 also occurs through the vertical buoyancy flux

$$VBF = \overline{w'b'}. \quad (22)$$

429 All the production terms are normalized by $C_d^*V_0^3$, a commonly used scaling (Sen et al.,
 430 2008; Arbic et al., 2009; Ruan, Wenegrat, & Gula, 2021) for energy dissipation within a flat
 431 bottom turbulent BBL with bottom stress $\rho_0C_d^*V_0^2$, where C_d^* is again taken to be 0.0022. Fig.
 432 7 shows that conversion of energy from the mean flow to the eddies on the anticyclonic side
 433 is accomplished primarily by VRS and VBF at $\hat{h} = 1.6$, and through a combination of VRS,
 434 HRS and VBF at $\hat{h} = 3.2$. In the dynamical framework of Thomas et al. (2013) and Wenegrat
 435 and Thomas (2020), the former may be classified as a hybrid symmetric/gravitational insta-
 436 bility and the latter a hybrid symmetric/centrifugal/gravitational instability. The instability tends
 437 to restratify the BBL, bringing the flow back toward a state of marginal stability $q \approx 0$ (Fig.
 438 6b,c). VBF is primarily responsible for the restratification, converting available potential en-
 439 ergy to EKE in the process. Note that the large VBF contribution well downstream of the ridge
 440 centerline may also indicate the presence of a hybrid baroclinic mode on the anticyclonic side.
 441 The restratification in the BBL and the corresponding reduction in the geostrophic vertical shear
 442 can be seen in the last panel of Fig. 4 ($y/a = 43$). For the larger \hat{h} cases, partial restratifica-
 443 tion of the BBL following the onset NPV instabilities manifests as a net sink in the Lagrangian
 444 vertical shear equation (black line in bottom panel of Fig. 5).

445 On the cyclonic side, EKE production is overwhelmingly from HRS, and is substantially
 446 more intense compared to the anticyclonic side. This is strongly indicative of a horizontal, in-
 447 flectional point instability of the mean flow, similar to that seen, for example, in submesoscale
 448 and BBL resolving simulations of topographic wakes in the Southwestern Pacific (Srinivasan
 449 et al., 2017). VBF, which acts as minor sink of EKE, represents conversion from EKE to avail-
 450 able potential energy resulting from the upslope advection of buoyancy. Fig. 7 also shows that
 451 HRS conversion commences further upstream for the $\hat{h} = 3.2$ case compared to $\hat{h} = 1.6$. The

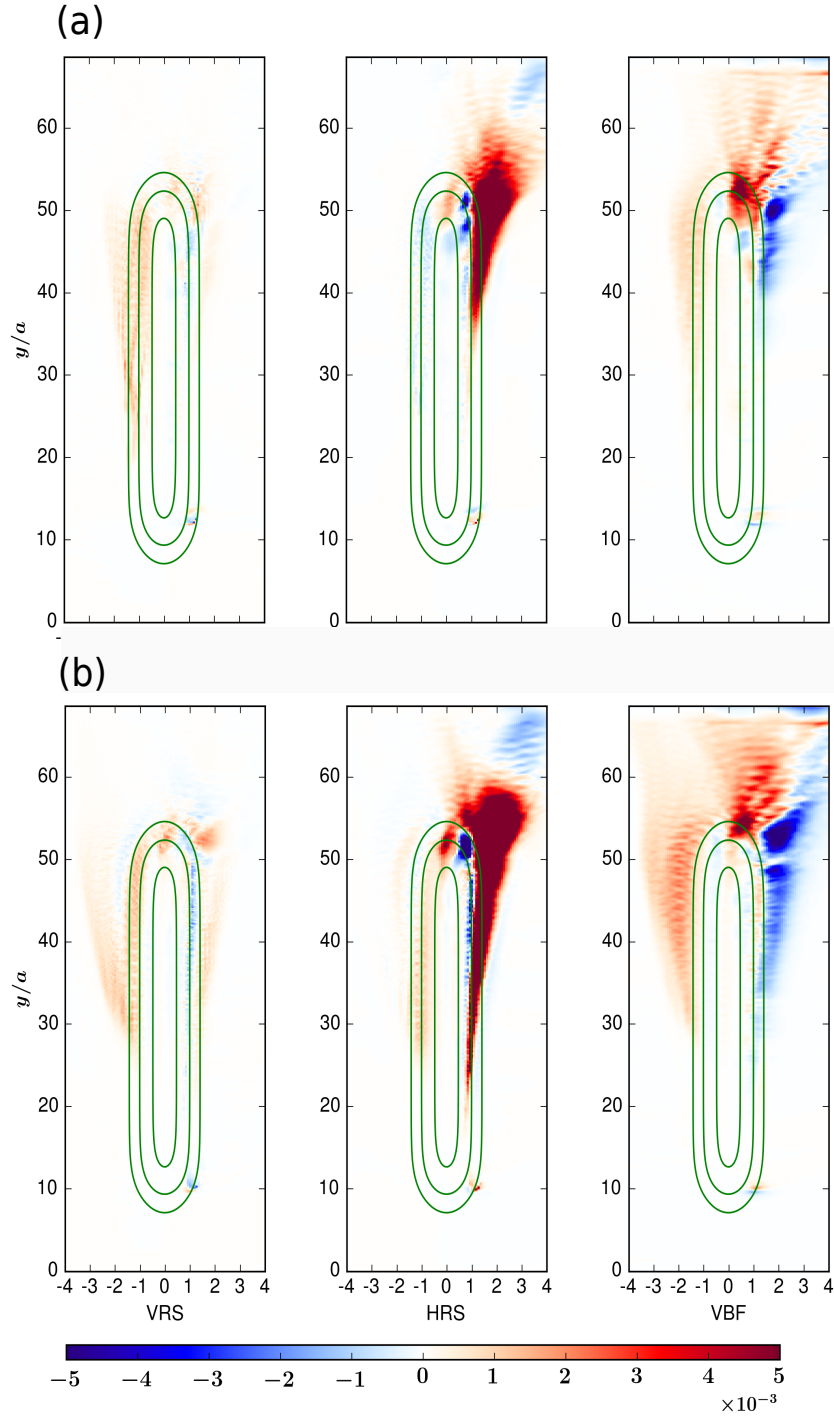


Figure 7. Time-averaged, vertically integrated EKE production terms (Eqs. (20), (21) and (22) for (a) $\hat{h} = 1.6$ and (b) $\hat{h} = 3.2$. A Gaussian filter has been applied to VBF to remove grid scale noise downstream of the ridge. All quantities are non-dimensionalized by $C_d^* V_0^3$, with $C_d^* = 0.0022$, and the colormap is saturated at 6×10^{-1} .

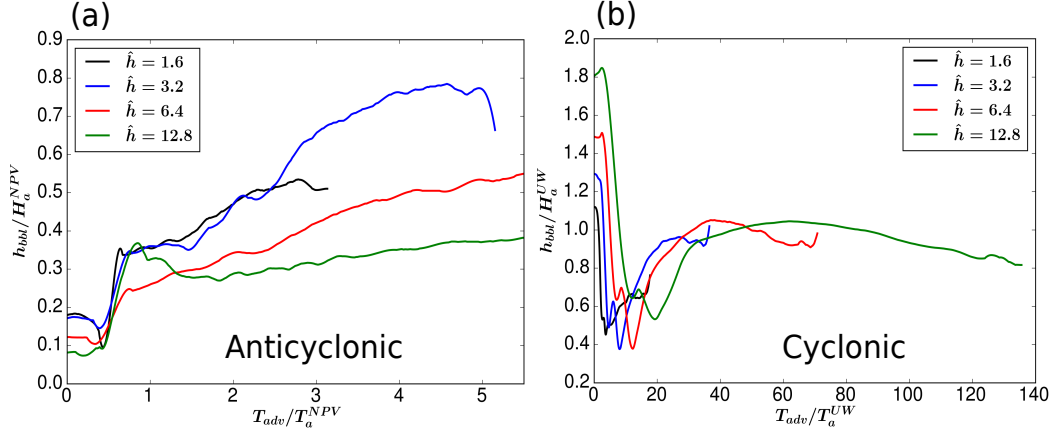


Figure 8. (a) Evolution of the cross-slope averaged BBL depth h_{bbl} as a function of the advective time T_{adv} . Recall that $T_{adv} = (s - s_0)/V_0$ is the along-streamline distance expressed as a time scale. (a) On the anticyclonic side, normalized by the Wenegrat and Thomas (2020) prediction for the arrest height (Eq. (13)) when NPV instabilities are active. (b) On the cyclonic side, normalized by the Brink and Lentz (2010a) prediction (Eq. (14)) for an upwelling Ekman layer

452 onset of horizontal barotropic instability on the topographic slopes could partly explain why
 453 the strip of cyclonic vorticity generated through the Bottom Stress Divergence Torque (Jagannathan
 454 et al., 2021) detaches from the slopes further upstream compared to the anticyclonic side. As
 455 seen in Fig. 2b,d, for all \hat{h} considered, the early separation reverses the decaying trend of bot-
 456 tom stress on the cyclonic side, past $s/a \approx 20$ (where s is the along-streamline distance).

457 As in the case of observations by Garabato et al. (2019) and solutions of Wenegrat and
 458 Thomas (2020), the BBL on the downwelling (anticyclonic) side remains substantially strat-
 459 ified in our solutions (Fig. 6a). Recall the definition of the BBL on the downwelling side as
 460 the height from the bottom where the stratification first exceeds $1.1N^2\hat{h}^2/(1+\hat{h}^2)$ (see sec-
 461 tion 4.1). In Fig. 8a we show the downstream evolution of the across-slope averaged BBL thick-
 462 ness h_{bbl} on the anticyclonic side. The values are non-dimensionalized using the predicted value
 463 of NPV instability - modulated arrest height in Wenegrat and Thomas (2020) (Eq. (13)). The
 464 BBL deepens downstream as the flow evolves along the slopes, but in all cases, its depth is
 465 less than the predicted value when the current separates off the slopes. On the cyclonic side,
 466 the stabilizing effect of upslope buoyancy advection is expected to shrink the boundary layer
 467 thickness, relative to the upstream flat-bottom value (Brink & Lentz, 2010a). Fig. 8b shows
 468 that h_{bbl} decreases sharply during the initial encounter, even beyond the value predicted in Brink

469 and Lentz (2010a). Further downstream, h_{bbl} slowly approaches H_a^{UW} . However, as noted ear-
 470 lier, the separation of the current from the slopes and the slow increase observed in the bot-
 471 tom stress (Fig. 2b,d) are indicative of the BBL not being fully arrested.

472 The loss of energy due to dissipation can be partitioned into that from the mean kinetic
 473 energy (MKE) of the parameterized BBL turbulence, $\bar{\epsilon}$, and that due to the forward cascade
 474 initiated by the ageostrophic instabilities, ϵ' . Recall that eddy dissipation in ROMS occurs through
 475 both the parameterized vertical Reynolds stress τ_z as well as a horizontal hyperdiffusion term
 476 that is implicit in the third order upwind biased scheme for computing horizontal advection.
 477 To quantify the influence of the topography on dissipation, $\bar{\epsilon}$ and ϵ' are defined here as area
 478 averages over the sloping sides of the ridge. For example on the anticyclonic side,

$$\bar{\epsilon} = \frac{\iint_A \int_{-H}^{-H+h_{bbl}} \bar{\mathbf{u}} \cdot (\overline{\tau_z} + \overline{\mathcal{D}_H \mathbf{u}}) dz dy dx}{\iint_A dy dx} \quad (23a)$$

$$\epsilon' = \frac{\int_{-\infty}^0 \int_{-\infty}^{\infty} \int_{-H}^{\eta} \overline{\mathbf{u}' \cdot (\tau'_z + \mathcal{D}_H \mathbf{u}')} dz dy dx}{\iint_A dy dx}, \quad (23b)$$

480 where η is the sea surface elevation, \mathcal{D}_H denotes the horizontal hyperdiffusion term on the
 481 RHS of the horizontal momentum equations. A is the region bounded by the y -axis and some
 482 low-level bathymetric contour, here taken to be the contour on which the ridge height decays
 483 to $\exp(-2)$ of its maximum value h_m ,

$$A = \{x, y | x \leq 0; h(x, y) > h_m \exp(-2)\}, \quad (24)$$

484 The dissipation fractions $\bar{\epsilon}$ and ϵ' and slope region A are defined analogously for the cyclonic
 485 side.

486 Eq. (23a) represents the area-averaged MKE dissipation from the BBL over the slop-
 487 ing sides of the ridge. The ‘slope effect’ on BBL dissipation is visible when we plot $\bar{\epsilon}$ nor-
 488 malized by $C_d^* V_0^3$ (Fig. 9a) for each \hat{h} solution. For $\hat{h} = 1.6$, the dissipation rate of MKE on
 489 the anticyclonic side is around 75% of that expected from the flat-bottom scaling $C_d^* V_0^3$, re-
 490 flective of moderate bottom stress reduction. As \hat{h} increases, the normalized $\bar{\epsilon}$ decreases, falling
 491 to as low as 0.1 for $\hat{h} = 12.8$. The diminished $\bar{\epsilon}$ is indicative of partial arrest of the BBL.

492 The numerator of Eq. (23b) is the volume integral of the EKE dissipation over the to-
 493 tal fluid volume on the anticyclonic side and not just within the BBL as is the case in Eq. (23a).
 494 This choice reflects the fact that the instabilities spawned on the slopes give rise to eddies which
 495 generally dissipate over a broad wake region rather than locally (c.f. Srinivasan et al., 2021).
 496 Dividing the total eddy-induced dissipation by $\iint_A dy dx$ thus specifically captures the effect

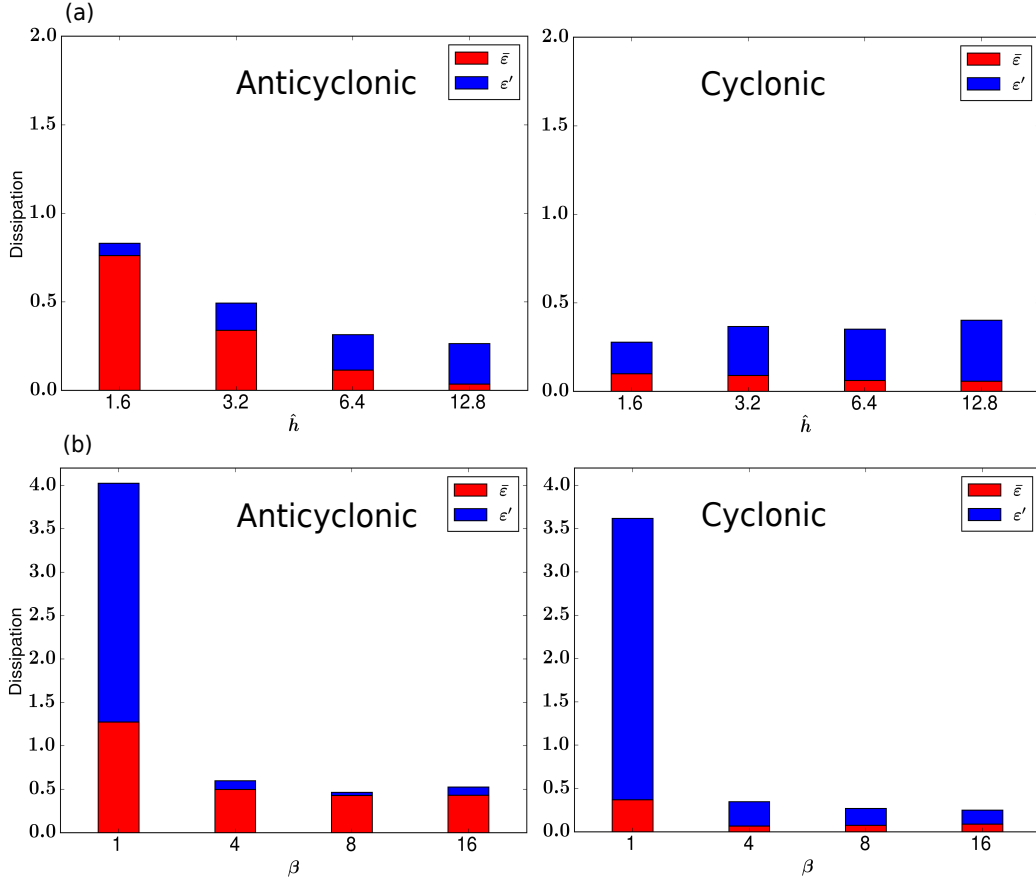


Figure 9. Barplot showing separate contributions of $\bar{\epsilon}$ and ϵ' , defined in Eqs. (23a) and (23b), to the energy dissipation on each side of the ridge. The integrals have been normalized by $C_d^* V_0^3$ with $C_d^* = 0.0022$, the usual scaling for the depth integrated dissipation rate in a turbulent BBL with far-field velocity V_0 (Sen et al., 2008; Arbic et al., 2009). (a) Elongated ridge with varying \hat{h} and (b) Elliptical ridge at fixed $\hat{h} = 3.2$ and varying aspect ratio β .

497 of the slope-current encounter on energy dissipation. That is, it tells us how much EKE dis-
 498 sipation occurs as a result of slope-current interactions over a unit area on the anticyclonic side
 499 of the ridge. Wenegrat and Thomas (2020) predicted using theoretical scalings that in a 2D
 500 downwelling BBL undergoing arrest, NPV instabilities offset exactly half of the *reduction* in
 501 the energy dissipation caused by Ekman arrest. Here we find that ϵ' on the anticyclonic side
 502 increases from around 0.05 at $\hat{h} = 1.6$ to around 0.2 at $\hat{h} = 12.8$. Thus while dissipation due
 503 to SI/CI amounts to between 5% and 20% of the expected flat-bottom BBL dissipation, it is
 504 nevertheless considerably smaller in our solutions compared to the Wenegrat and Thomas (2020)
 505 scaling.

506 On the cyclonic side, $\bar{\epsilon}$ is below 0.1 for all \hat{h} while ϵ' is around 0.3 at the largest \hat{h} . Thus
 507 dissipation resulting from the horizontal inflectional point instability outstrips that due to the
 508 bottom drag for all but the lowest \hat{h} considered. In conclusion, on both sides of the ridge, EKE
 509 dissipation compensates a fraction of the reduction in dissipation resulting from partial arrest
 510 of the turbulent BBL on the slopes — between 5% and 20% on the anticyclonic side and up
 511 to 30% on the cyclonic side, depending on the value of \hat{h} .

512 A caveat to the above observations regarding NPV and dissipation concerns the horizon-
 513 tal resolution used (300 m). Note that locally, we can estimate the horizontal scale of sym-
 514 metric instability modes from Taylor and Ferrari (2009) as

$$L = h_{bbl} / \theta_{iso}, \quad (25)$$

515 where θ_{iso} is the isopycnal slope within the BBL. In Fig. 10, we display the absolute values
 516 of the isopycnal slope on the anticyclonic side for the case $\hat{h} = 3.2$. Note that at $y/a = 27$,
 517 which is around where the NPV instabilities become prominent in snapshots of integrated vorticity
 518 (Fig. 1), $|\theta_{iso}|$ in the BBL is largely in the range of 0.1 or less, except very near the bot-
 519 tom where it approaches unity. The isopycnal slopes are very similar for the other \hat{h} and hence
 520 not shown.

521 Substituting the values of V_0 , \hat{h} and N for our runs in Eq. 13 gives theoretical arrest heights
 522 ranging from ≈ 220 m for $\hat{h} = 1.6$, to ≈ 160 m for the $\hat{h} = 12.8$. From inspection of Fig. 8,
 523 this gives values of h_{bbl} before separation from the ridge, of around 165 m for $\hat{h} = 1.6$, 65
 524 m for $\hat{h} = 12.8$ and around 90 m for each of the cases $\hat{h} = 3.2$ and 6.4. From Eq. (25), this
 525 implies a horizontal scale of the symmetric instability mode $L \approx 1650$ m for $\hat{h} = 1.6$, 900 m
 526 for $\hat{h} = 3.2$ and 6.4 and 650 m for the largest \hat{h} of 12.8 considered here. Thus with a hori-
 527 zontal resolution of 300 m, our simulations capture the onset of symmetric instability, but do
 528 not resolve their evolution to finite amplitude and subsequent equilibration via secondary Kelvin-
 529 Helmholtz instability (Taylor & Ferrari, 2009). Consequently it is likely that the dissipation
 530 rates obtained here underestimate the true rate of energy dissipation in hybrid NPV, particu-
 531 larly for large \hat{h} .

532 **5 The effect of ridge curvature**

533 The elongated ridge (Fig. 1) was specifically chosen for this study as it represents a par-
 534 ticularly favorable configuration for observing 1D-like buoyancy adjustment in a 3D setting.
 535 With curvature and/or shorter ridge length, the evolution to Ekman arrest is expected to be vi-

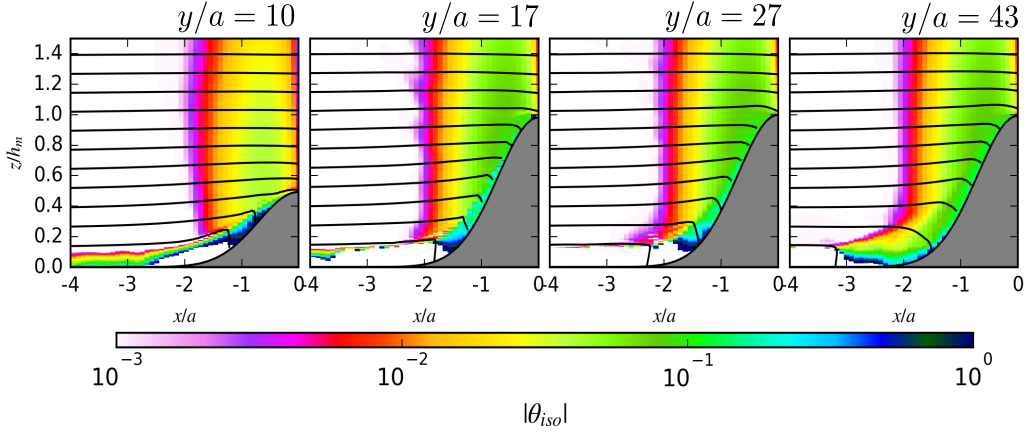


Figure 10. Downstream evolution of the time-averaged isopycnal slope $|\theta_{iso}|$ on the anticyclonic (downwelling) side where symmetric instability modes are present, for the $\hat{h} = 3.2$ solution. Also overlain are the mean flow isopycnals. Note that, except very close to the boundary, $|\theta_{iso}|$ is largely $\mathcal{O}(0.1)$ or smaller adjacent to the ridge slope.

536 initiated by vortical dynamics and agesotrophic instabilities. To demonstrate how this may hap-
 537 pen, we have performed additional simulations for elliptical ridges with varying lateral aspect
 538 ratio $\beta = b/a$, where a and b are respectively, the cross-flow and along-flow dimensions of
 539 the ridge. \hat{h} is set to 3.2 in all these runs. Fig. 11 shows the time-averaged bottom stress and
 540 instantaneous snapshots of integrated vorticity for three cases corresponding to $\beta = 1, 4$ and
 541 16. Compared to the elongated ridge (Fig. 1), the bottom stress here exhibits less of a system-
 542 atic downstream pattern; rather stress reduction is patchy and spatially intermittent. As also
 543 seen in the former, bottom stress divergence torque (Jagannathan et al., 2021) acting on the
 544 slopes, generates vorticity, which upon flow separation leads to the emergence of highly co-
 545 herent vortical wakes.

546 As we shall see below, for small-to-moderate aspect ratios β , the NPV instability on the
 547 anticyclonic side is dominated by centrifugal rather than symmetric modes, i.e. the NPV comes
 548 mainly from the vertical component of PV, $q_v = (\zeta + f)b_z$, where ζ is the relative vertical
 549 vorticity. For this reason, the symmetric instability criterion of Allen and Newberger (1996)
 550 is not the most appropriate choice for defining the BBL height for the elliptical ridge solutions.
 551 To enable consistent comparison between the different β cases, we instead define the BBL height
 552 here as the depth over which the stratification is smaller than N^2 . The downstream evolution
 553 of the BBL height is shown in Fig. 12. For a circular ridge ($\beta = 1$), the encounter time along

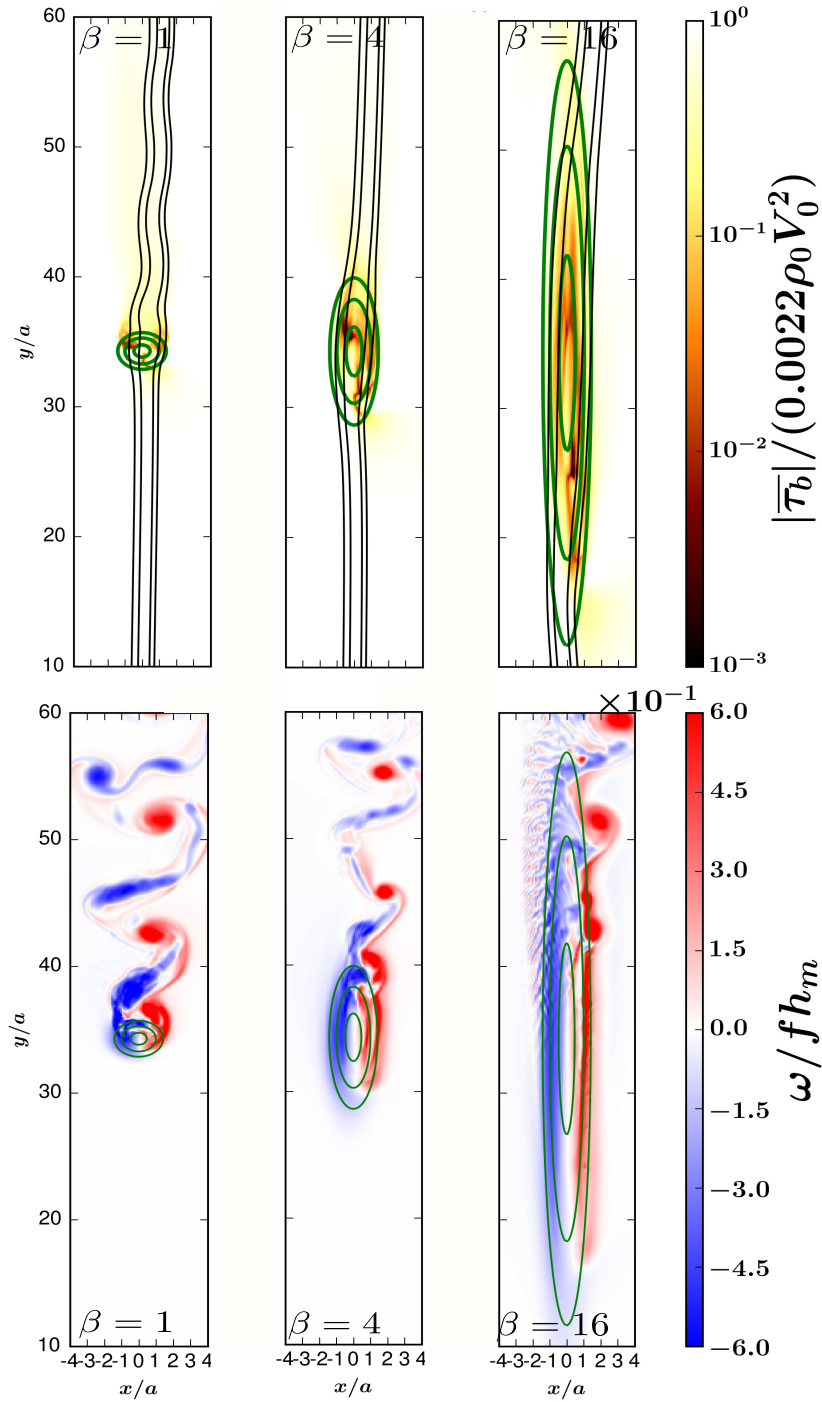


Figure 11. Same as Fig. 1 but for elliptical shaped ridges with varying aspect ratio β , at a fixed $\hat{h} = 3.2$. Note that the small scale eddying structures on the anticyclonic side for $\beta = 16$ case mirror similar structures seen in the case of the elongated ridge (Fig. 1)

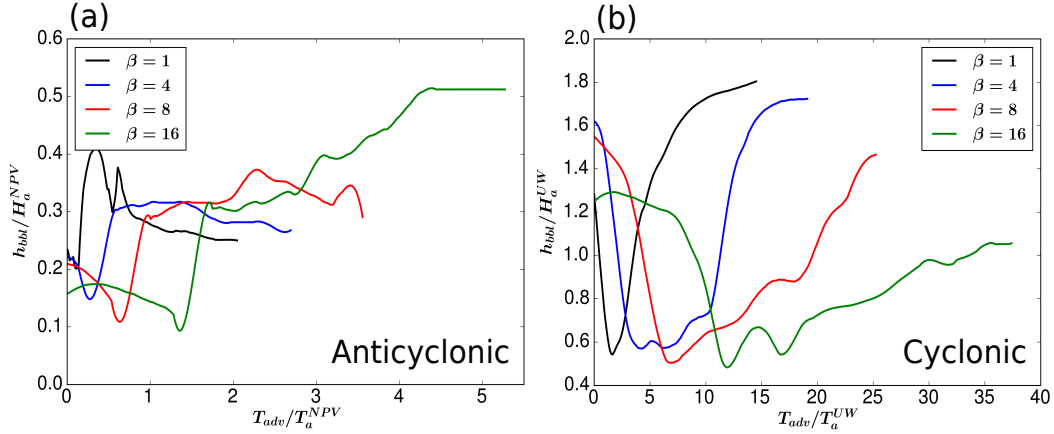


Figure 12. Same as Fig. 8 but for the elliptical ridge solutions. (a) Anticyclonic side and (b) Cyclonic side.

554 the slopes is insufficient for sustained buoyancy adjustment to occur. For $\beta = 4$ and higher,
 555 the BBL on the anticyclonic side deepens downstream following a sharp contraction during
 556 the initial encounter with the ridge. The deepening BBL is evidence of convective mixing, sim-
 557 ilar to what occurs over the elongated ridge (Fig. 8); this is particularly evident for the $\beta =$
 558 16 case. On the cyclonic side, the evolution of the BBL is similar in most respects to that ob-
 559 served over the elongated ridge (Fig. 2). The BBL height shrinks on the slopes due to the sta-
 560 bilizing effect of upslope Ekman transport as predicted in Brink and Lentz (2010a) and seen
 561 in Fig. 8 above. In all cases the BBL subsequently rebounds toward its pre-encounter height.

562 A notable aspect of these solutions concerns the EKE production and dissipation on the
 563 anticyclonic side. Fig. 13 reveals that the energy conversion terms are an order of magnitude
 564 larger in the case of $\beta = 1$ compared to $\beta = 16$. Focussing on the anticyclonic side, EKE pro-
 565 duction for $\beta = 1$ is predominantly due to HRS and occurs downstream of the ridge. Com-
 566 bined with the fact that the anticyclonic eddies are associated with NPV anomalies, this is in-
 567 dicative of centrifugal instability. By contrast, for $\beta = 16$, energy transfer from the mean flow
 568 to the eddies occurs through a combination of HRS, VRS and VBF. Furthermore, VRS pro-
 569 duction in this case begins on the slopes (Fig. 13), indicating that the instability emerges even
 570 as the BBL is evolving on the slopes. We identify this as a hybrid centrifugal/symmetric/gravitational
 571 mode of instability, similar to that seen in the $\hat{h} = 3.2$ elongated ridge solution (Figs. 1,7). This
 572 hybrid mode is characterized by a smaller horizontal scale than the $\beta = 1$ solution, as is vi-
 573 sually evident (e.g. in Fig. 11).

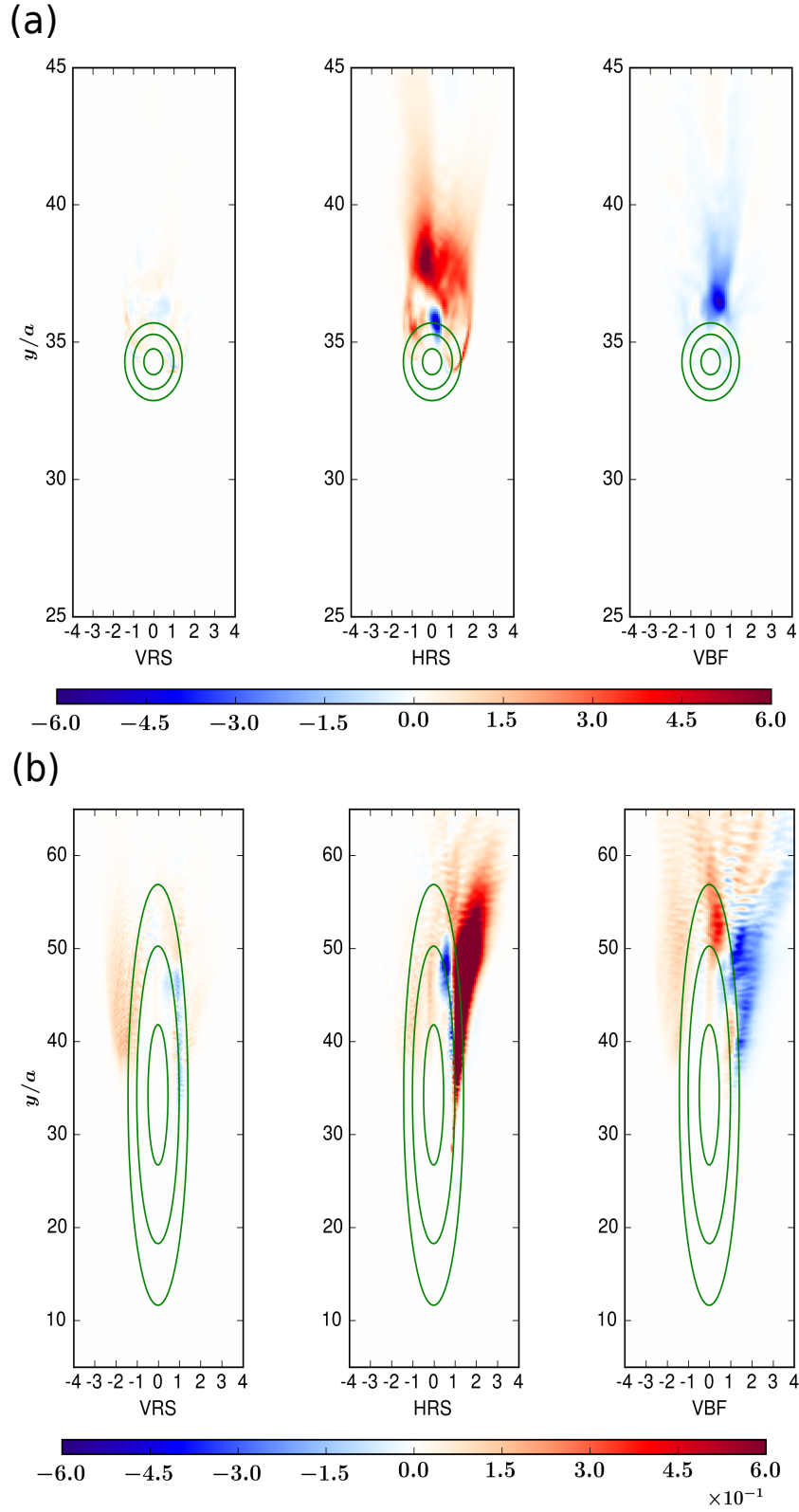


Figure 13. Same as Fig. 7 but for the elliptical ridge solutions. (a) $\beta = 1$ and $\beta = 16$. The EKE production is much higher for $\beta = 1$; accordingly the colomap is saturated at 5×10^{-2} in (a) and 5×10^{-3} in (b).

574 A direct consequence of the shifting EKE production patterns on the anticyclonic side is
 575 on the zonally, and depth integrated dissipation rate of EKE $\int_{-\infty}^0 \int_{-H}^{\eta} \overline{\mathbf{u}' \cdot (\boldsymbol{\tau}'_z + \mathcal{D}\mathbf{u}')}$ dz dx. As
 576 a function of aspect ratio, Fig. 14b shows that energy dissipation is highest for $\beta = 1$, decreases
 577 as β increases through to 8, and again increases for $\beta = 16$. From Fig. 13, we may interpret
 578 this result as follows. As the aspect ratio of the ridge increases from $\beta = 1$ to 8, there is a
 579 transition from a highly dissipative centrifugal instability to a more modestly dissipative one.
 580 As the curvature decreases further (or the encounter length increases), there is more time for
 581 buoyancy adjustment on the slopes. The resulting increase in the geostrophic vertical shear
 582 renders the slow unstable to a hybrid centrifugal/symmetric/gravitational mode which enhances
 583 turbulent dissipation. For comparison, the EKE dissipation rate in the elongated ridge solu-
 584 tions (Fig. 14a) exhibits a monotonic increasing trend with \hat{h} .

585 The overall contribution of ε' to the total energy dissipation is highest for the circular
 586 ridge (Fig. 9b). The normalized total dissipation rate in this case is over 3.5 in an area-averaged
 587 sense, with bottom drag dissipation $\bar{\varepsilon}$ around 1.3 and 0.4 respectively on the anticyclonic and
 588 cyclonic sides — an indication that buoyancy adjustment effects are small. The bottom drag
 589 dissipation on the anticyclonic side is around 0.5 for $\beta = 4$ and higher and the total dissipa-
 590 tion rate itself also remains below 1. This is roughly in line with the recent findings of Ruan,
 591 Wenegrat, and Gula (2021) who find that geostrophic shear in the BBL reduces energy dis-
 592 sipation by at least 56% in a high-resolution model of the Atlantic. On the cyclonic side, the
 593 total dissipation rate ranges between 0.28 and 0.35 as β goes from 4 to 16, energy loss due
 594 to bottom drag is diminished by as much as 90% relative to the flat bottom scaling and ε' com-
 595 prises a much larger fraction of the total dissipation compared to the anticyclonic side.

596 6 Discussion

597 6.1 Temporal Vs spatial evolution of buoyancy adjustment

598 We have examined the process of bottom stress reduction and buoyancy adjustment within
 599 the BBL in a 3D setting of barotropic inflow encountering an elongated ridge. In section 4.1,
 600 we analyzed the quasi-temporal evolution of the bottom stress along the slopes by defining an
 601 advective time scale T_{adv} and scaling this with $T_a NPV$ and T_a^{UW} . The implicit assumption be-
 602 hind this scaling was an approximate equivalence between the downstream evolution of the
 603 BBL along the ridge slopes, and temporal evolution in 1D and 2D (as in Brink & Lentz, 2010a;
 604 Wenegrat & Thomas, 2020). Using an idealized theoretical model with a linear bottom drag,

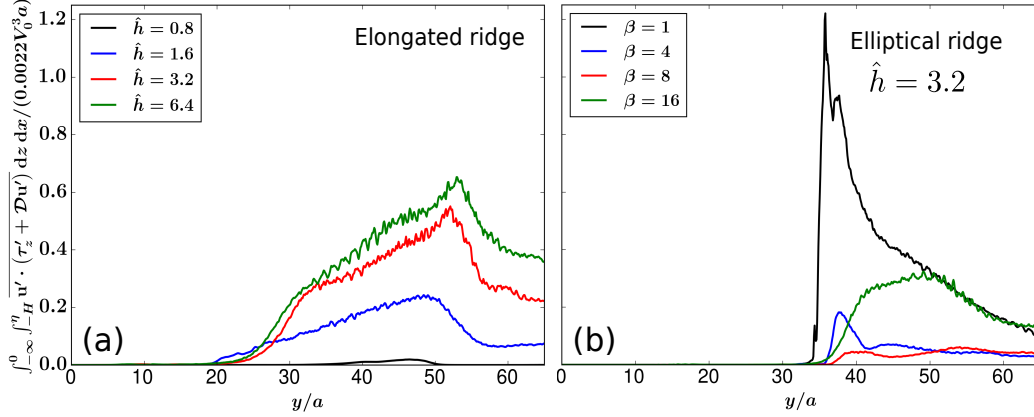


Figure 14. Downstream evolution of the zonally, and depth integrated dissipation rate

$\int_{-\infty}^0 \int_{-H}^{\eta} \mathbf{u}' \cdot (\boldsymbol{\tau}'_z + \mathcal{D}_H \mathbf{u}') dz dx$ of EKE corresponding to the eddying flow component on the anticyclonic side. (a) elongated ridge solutions at different values of \hat{h} and (b) elliptical ridge solutions with varying β , at a fixed value of $\hat{h} = 3.2$. The values have been normalized by $C_d^* V_0^3 a$ with $C_d^* = 0.0022$, the expected dissipation rate within a turbulent BBL over a horizontal width a .

605 Chapman and Lentz (1997) found that although this assumption does not strictly hold in the
 606 case of initially narrow currents, the evolution of a wide current over a sloping bottom is es-
 607 sentially 1D downstream, with along-isobath distance playing the role of time. Here we find
 608 that non-linear straining effects during the current-topographic encounter results in a rapid ini-
 609 tial adjustment of the BBL and significant stress reduction over advective times $T_{adv} < T_a^{NPV}$
 610 (Fig. 2c and Fig. 5). Further, the quadratic bottom drag in our simulations, instabilities, sec-
 611 ondary circulations, and early flow separation (on the cyclonic side) mean that the evolution
 612 of the BBL in the downstream direction departs considerably from the expectation of quasi-
 613 temporal 1D evolution of Chapman and Lentz (1997).

6.2 Sensitivity to choice of BBL parameterization

614
 615 Much of the previous work exploring buoyancy adjustment over slopes have utilized ei-
 616 ther a $k-\epsilon$ closure (Brink & Lentz, 2010a), 2.0 or 2.5 level Mellor-Yamada closure (Brink
 617 & Lentz, 2010a; Benthuisen et al., 2015) for parameterizing BBL turbulence. Recently, LES
 618 have also been employed for this purpose (Ruan et al., 2019; Ruan, Thompson, & Taylor, 2021;
 619 Wenegrat & Thomas, 2020). Wijesekera et al. (2003) carried out a systematic comparison of
 620 $k-\epsilon$, Mellor-Yamada 2.5 and KPP mixing in modelling the structure of vertical mixing over

621 a continental shelf forced by either upwelling- or downwelling-favorable winds. Although they
 622 note some quantitative differences in the vertical profiles of eddy viscosity and diffusivity, the
 623 shape and structure of these mixing coefficients was similar across all three schemes, with lo-
 624 cal maxima in the surface and bottom boundary layers and a smooth connection to the inte-
 625 rior. In particular, they find that all three models produce a similar BBL thickness and ver-
 626 tical profiles of velocity and density. In another study, Bachman et al. (2017) found that when
 627 the shear instability component of KPP is included, the total turbulence production compares
 628 favorably with LES solutions even though individual components may sometimes be overes-
 629 timated. All the simulations here are performed with the shear instability component of KPP
 630 included and the critical Richardson number set to 0.45. Thus taking a statistical steady state
 631 view that turbulence production must equal dissipation in a volume integral sense, KPP is un-
 632 likely to be a major source of error in our dissipation calculations.

633 **6.3 Distinguishing Ekman arrest and turbulence collapse**

In their LES solutions with periodic boundary conditions in the cross- and along- slope
 directions, Ruan et al. (2019); Ruan, Thompson, and Taylor (2021) observe that, both in the
 downslope and upslope regime, the BBL always relaminarizes before an arrested state is reached.
 This is a consequence of suppression of turbulence by the cross-slope buoyancy flux, a phe-
 nomenon which the authors characterize using a so-called slope-Obukhov length scale, defined
 as

$$L_s = \frac{-u_0^{*3}}{\kappa U_E N^2 \theta}. \quad (26)$$

634 In Eq. (26), θ is the slope angle and $U_E N^2 \theta$ is the cross-slope Ekman buoyancy flux. Given
 635 a molecular viscosity ν , Ruan et al. (2019); Ruan, Thompson, and Taylor (2021) find that tur-
 636 bulence collapse occurs when $L_s u^* / \nu$ falls below a threshold, around 100. However in the 2D
 637 solutions of Wenegrat and Thomas (2020), where both submesoscale instabilities and the near-
 638 wall layer are adequately resolved, the onset of NPV instabilities appears to prevent a relam-
 639 inarized state from being attained.

640 As shown in Flores and Riley (2011), turbulence collapse occurs when there is insuf-
 641 ficient scale-separation between the $\mathcal{O}(L)$ and $\mathcal{O}(\nu/u^*)$ scales of turbulent motions in the dy-
 642 namic sublayer, where L is the Obukhov length and ν is the molecular viscosity. Here we do
 643 not explicitly resolve the dynamic sublayer, but rather rely on a turbulent bottom drag param-
 644 eterization. Thus turbulence collapse in our solutions, if it occurs, would imply $u_0^* \rightarrow 0$. How-

645 ever since buoyancy adjustment itself leads to substantial reduction of the bottom stress, we
 646 note that it is difficult to distinguish Ekman arrest from turbulence collapse. Fully 3D LES or
 647 DNS solutions are needed to understand if and how BBL relaminarization manifests over 3D
 648 bottom topography. We note however that, because EKE production is enhanced on both sides
 649 of the ridge following the onset of NPV instabilities (anticyclonic) and barotropic (cyclonic)
 650 instability modes (Fig. 10 above and Fig. 16 of Jagannathan et al. (2021)), EKE suppression
 651 as a proxy for identifying BBL relaminarization (as in as in Ruan et al. (2019)), may not be
 652 as useful in 3D.

653 **7 Summary and conclusion**

654 We have examined the process of buoyancy adjustment on 3D topography by analyz-
 655 ing a set of idealized ROMS simulations of an initially uniform upstream flow past ridges with
 656 and without boundary curvature. Key metrics such as the extent of reduction of the bottom
 657 stress, the BBL height and the observed adjustment time scales are discussed in the context
 658 of the 1D and 2D Ekman arrest literature. BBL turbulence in our solutions is parameterized
 659 using the K-profile parameterization (KPP) and the 300 m horizontal resolution employed re-
 660 solves submesoscale motions, including the onset of NPV instabilities on the anticyclonic side.
 661 Analyzing the EKE budget, we further diagnose the nature of the instabilities that develop over
 662 the course of the downstream BBL evolution on each side of the ridge, and the dissipation re-
 663 sulting thereof.

664 The evolution of the bottom stress in our solutions (Figs. 1 and 2) is to be contrasted
 665 with the 1D model runs of Brink and Lentz (2010a) and the more recent 2D simulations of
 666 Wenegrat and Thomas (2020) covering a range of slope Burger numbers. In their (constant-
 667 slope) solutions, buoyancy adjustment effects inexorably push the bottom stress towards zero.
 668 This occurs over a time scale corresponding to the time of mixed layer growth, either through
 669 upright or slantwise convection. For the \hat{h} values considered, the predicted arrest time scale
 670 T_a^{NPV} in Eq. (12) for a constant slope, ranges from 4 to 8 inertial periods for $\hat{h} = 12.8$ and
 671 1.6 respectively, with the smallest theoretical arrest time scale corresponding to the largest \hat{h}
 672 and vice-versa. Although there is a significant reduction of the stress on the slopes over these
 673 time scales (Fig. 2), analysis of the vertical shear equation shows that, contrary to 1D and 2D
 674 solutions where the stress reduction is purely due to the thermal wind shear induced by cross-
 675 slope buoyancy advection, here 3D nonlinear straining effects during the early encounter have
 676 an important role in the adjustment process.

677 The state of the BBL before separation, in the elongated ridge solutions, is character-
 678 ized by suppression of the bottom stress by between 60% ($\hat{h} = 1.6$) to 95% ($\hat{h} = 12.8$) on the
 679 anticyclonic side with respect to the upstream flat-bottom value (Fig. 2a,c), and up to 80% re-
 680 duction on the cyclonic side (Fig. 2b,d) for all \hat{h} . On the anticyclonic side, the stress has ei-
 681 ther plateaued or is decaying only slowly when the current separates (Fig. 2a,c). This is pos-
 682 sibly due to the influence of secondary circulations that feedback into the interior along-slope
 683 flow, as was noted in Benthuisen et al. (2015). The depth of the BBL on the anticyclonic side
 684 also remains well below the 2D prediction of Wenegrat and Thomas (2020). On the cyclonic
 685 side, early separation reverses the decaying trend of bottom stress within a short distance down-
 686 stream of the encounter (Fig. 2b,d). Thus on either side of the ridge, we may characterize the
 687 BBL as being in a state of ‘partial arrest’.

688 Our solutions demonstrate an inverse relationship between the drag-mediated energy dis-
 689 sipation rate and non-dimensional ridge height \hat{h} as well as lateral aspect ratio β (Fig. 9) —
 690 a consequence of increasing geostrophic BBL shear and reduced near-bottom velocities. This
 691 reduction in the bottom drag dissipation is somewhat compensated by dissipation arising from
 692 ageostrophic instabilities on either side, but to a lesser extent than predicted by Wenegrat and
 693 Thomas (2020). The exception is the circular ridge ($\beta = 1$) solution (Figs. 9b,14b) where the
 694 dissipation on both sides is significantly enhanced relative to the flat bottom BBL.

695 The fact that the bottom stress, energy dissipation and Ekman transport weaken substan-
 696 tially on the slopes of the ridge (Figs. 1 and 3) would suggest that partial Ekman arrest may
 697 be a fairly common occurrence in boundary currents adjacent to the continental shelf. Yet oceanic
 698 observations of Ekman arrest remain scarce, a notable exception being the Northern Califor-
 699 nia Shelf observations of Lentz and Trowbridge (2001). One possible explanation for this is that,
 700 on realistic bathymetry, curvature and irregular, small scale features such as headlands and bumps
 701 could trigger localized flow separation and reattachment events. This can be seen in the Cal-
 702 ifornia Undercurrent (CUC). For example, Fig. 5 of Molemaker et al. (2015) shows eddies roll
 703 up and separate all along the coast, but especially around Point Sur. If such events sporadi-
 704 cally punctuate the flow evolution on the slopes, they could potentially undermine the buoy-
 705 ancy adjustment process. Another plausible explanation for the paucity of observational data
 706 showing Ekman arrest, is the intrinsic temporal variability in the real ocean due to tides, wind-
 707 variability, coastally trapped waves and eddies impinging from offshore. In a 1D model with
 708 realistic broadband forcing, Brink and Lentz (2010b) find that the steady component of the
 709 flow undergoes Ekman arrest over time scales consistent with Eqs. (9) and (16), and further

710 that the bottom stress is also reduced across nearly all frequencies. Further studies with a well-
 711 resolved BBL are needed to understand how 3D effects like curvature, alongshore advection
 712 and realistic forcing influence the dynamics of Ekman adjustment in oceanic boundary cur-
 713 rents.

714 **Acknowledgments**

715 This work was made possible by the Office of Naval Research grant N00014-18-1-2599. Com-
 716 puting support was provided by the Extreme Science and Engineering Discovery Environment
 717 (XSEDE), which is supported by National Science Foundation grant number ACI-1548562.
 718 ALS was supported by the National Science Foundation under Grant Number OCE-1751386.

719 **Data Availability Statement**

720 The numerical model simulations upon which this study is based are too large to archive
 721 or to transfer. Instead, we provide all the information needed to replicate the simulations; we
 722 used the hydrostatic UCLA version of the Regional Ocean Modelling System (ROMS) to per-
 723 form the simulations. The model code, compilation script, initial and boundary condition files,
 724 and the namelist settings are available at <https://github.com/arjunj87/ROMS-ridge-solutions>.

725 **References**

- 726 Allen, J., & Newberger, P. (1996). Downwelling circulation on the oregon continental shelf.
 727 part i: Response to idealized forcing. *J. Phys. Oceanogr.*, *26*(10), 2011–2035.
- 728 Arbic, B. K., Shriver, J. F., Hogan, P. J., Hurlburt, H. E., McClean, J. L., Metzger, E. J., . . .
 729 Wallcraft, A. J. (2009). Estimates of bottom flows and bottom boundary layer dissipa-
 730 tion of the oceanic general circulation from global high-resolution models. *J. Geophys.*
 731 *Res: Oceans*, *114*(C2).
- 732 Armi, L. (1978). Some evidence for boundary mixing in the deep ocean. *J. Geophys. Res.: Oceans*, *83*, 1971–1979.
- 733 Armi, L., & D’Asaro, E. (1980). Flow structures of the benthic ocean. *J. Geophys. Res.: Oceans*, *85*(C1), 469–484.
- 734 Armi, L., & Millard Jr, R. C. (1976). The bottom boundary layer of the deep ocean. *J. Geo-*
 735 *phys. Res.*, *81*, 4983–4990.
- 736 Bachman, S. D., Fox-Kemper, B., Taylor, J. R., & Thomas, L. N. (2017). Parameterization of
 737 frontal symmetric instabilities. i: Theory for resolved fronts. *Ocean Modell.*, *109*, 72–
 738
 739

- 740 95.
- 741 Benthuisen, J., Thomas, L. N., & Lentz, S. J. (2015). Rapid generation of upwelling at a
742 shelf break caused by buoyancy shutdown. *J. Phys. Oceanogr.*, *45*(1), 294–312.
- 743 Brink, K. H., & Lentz, S. J. (2010a, Jan). buoyancy arrest and bottom ekman transport. part
744 I: Steady flow. *J. Phys. Oceanogr.*, *40*(4), 621–635.
- 745 Brink, K. H., & Lentz, S. J. (2010b, Dec). buoyancy arrest and bottom ekman transport. part
746 II: Oscillating flow. *J. Phys. Oceanogr.*, *40*(4), 636–655.
- 747 Chapman, D. C., & Lentz, S. J. (1997). Adjustment of stratified flow over a sloping bottom.
748 *J. Phys. Oceanogr.*, *27*(2), 340–356.
- 749 Flores, O., & Riley, J. (2011). Analysis of turbulence collapse in the stably stratified surface
750 layer using direct numerical simulation. *Bound.-Layer Meteorol.*, *139*(2), 241–259.
- 751 Garabato, A. C. N., Frajka-Williams, E. E., Spingys, C. P., Legg, S., Polzin, K. L., Forryan,
752 A., ... others (2019). Rapid mixing and exchange of deep-ocean waters in an abyssal
753 boundary current. *Proc. Natl. Acad. Sci.*, *116*(27), 13233–13238.
- 754 Garrett, C., MacCready, P., & Rhines, P. (1993). Boundary mixing and arrested ekman lay-
755 ers: Rotating stratified flow near a sloping boundary. *Annu. Rev. Fluid Mech.*, *25*(1),
756 291–323.
- 757 Gula, J., Molemaker, M., & McWilliams, J. (2015). Topographic vorticity generation, sub-
758 mesoscale instability and vortex street formation in the gulf stream. *Geophys. Res.*
759 *Lett.*, *42*(10), 4054–4062.
- 760 Hogg, N. G. (1973). On the stratified taylor column. *J. Fluid Mech.*, *58*(3), 517–537.
- 761 Jagannathan, A., Srinivasan, K., McWilliams, J. C., Molemaker, M. J., & Stewart, A. L.
762 (2021). Boundary-layer-mediated vorticity generation in currents over sloping
763 bathymetry. *J. Phys. Oceanogr.*, *51*(6), 1757–1778.
- 764 Large, W. G., McWilliams, J. C., & Doney, S. C. (1994). Oceanic vertical mixing: A review
765 and a model with a nonlocal boundary layer parameterization. *Rev. Geophys.*, *32*(4),
766 363–403.
- 767 Lentz, S., & Trowbridge, J. (2001). A dynamical description of fall and winter mean current
768 profiles over the northern california shelf. *J. Phys. Oceanogr.*, *31*(4), 914–931.
- 769 MacCready, P., & Rhines, P. B. (1991). Buoyant inhibition of ekman transport on a slope
770 and its effect on stratified spin-up. *J. Fluid Mech.*, *223*, 631–661.
- 771 McWilliams, J. C., Huckle, E., & Shchepetkin, A. F. (2009). Buoyancy effects in a stratified
772 ekman layer. *J. Phys. Oceanogr.*, *39*(10), 2581–2599.

- 773 Molemaker, M. J., McWilliams, J. C., & Dewar, W. K. (2015). Submesoscale instability and
 774 generation of mesoscale anticyclones near a separation of the California undercurrent.
 775 *J. Phys. Oceanogr.*, *45*(3), 613–629.
- 776 Orlandi, I. (1976). A simple boundary condition for unbounded hyperbolic flows. *J. Com-*
 777 *put. Phys.*, *21*(3), 251–269.
- 778 Perfect, B., Kumar, N., & Riley, J. (2018). Vortex structures in the wake of an idealized
 779 seamount in rotating, stratified flow. *Geophys. Res. Lett.*, *45*(17), 9098–9105.
- 780 Ruan, X., Thompson, A. F., & Taylor, J. R. (2019). The evolution and arrest of a turbu-
 781 lent stratified oceanic bottom boundary layer over a slope: Downslope regime. *J. Phys.*
 782 *Oceanogr.*, *49*(2), 469–487.
- 783 Ruan, X., Thompson, A. F., & Taylor, J. R. (2021). The evolution and arrest of a turbu-
 784 lent stratified oceanic bottom boundary layer over a slope: Upslope regime and pv
 785 dynamics. *J. Phys. Oceanogr.*
- 786 Ruan, X., Wenegrat, J. O., & Gula, J. (2021). Slippery bottom boundary layers: the
 787 loss of energy from the general circulation by bottom drag. *Geophys. Res. Lett.*,
 788 e2021GL094434.
- 789 Schär, C., & Davies, H. C. (1988). Quasi-geostrophic stratified flow over isolated finite am-
 790 plitude topography. *Dyn. Atmos. Oceans*, *11*(3-4), 287–306.
- 791 Sen, A., Scott, R. B., & Arbic, B. K. (2008). Global energy dissipation rate of deep-ocean
 792 low-frequency flows by quadratic bottom boundary layer drag: Computations from
 793 current-meter data. *Geophys. Res. Lett.*, *35*(9).
- 794 Shchepetkin, A. F., & McWilliams, J. C. (2003). A method for computing horizontal
 795 pressure-gradient force in an oceanic model with a nonaligned vertical coordinate. *J.*
 796 *Geophys. Res.: Oceans*, *108*(C3).
- 797 Shchepetkin, A. F., & McWilliams, J. C. (2005). The regional oceanic modeling system
 798 (roms): a split-explicit, free-surface, topography-following-coordinate oceanic model.
 799 *Ocean Modell.*, *9*(4), 347–404.
- 800 Srinivasan, K., McWilliams, J. C., & Jagannathan, A. (2021). High vertical shear and dissi-
 801 pation in equatorial topographic wakes. *J. Phys. Oceanogr.*
- 802 Srinivasan, K., McWilliams, J. C., Molemaker, M. J., & Barkan, R. (2019). Submesoscale
 803 vortical wakes in the lee of topography. *J. Phys. Oceanogr.*, *49*(7), 1949–1971.
- 804 Srinivasan, K., McWilliams, J. C., Renault, L., Hristova, H. G., Molemaker, J., & Kessler,
 805 W. S. (2017). Topographic and mixed layer submesoscale currents in the near-surface

- 806 southwestern tropical pacific. *J. Phys. Oceanogr.*, *47*(6), 1221–1242.
- 807 Taylor, J. R., & Ferrari, R. (2009). On the equilibration of a symmetrically unstable front via
808 a secondary shear instability. *J. Fluid Mech.*, *622*, 103–113.
- 809 Taylor, J. R., & Sarkar, S. (2008). Stratification effects in a bottom ekman layer. *J. Phys.*
810 *Oceanogr.*, *38*(11), 2535–2555.
- 811 Thomas, L. N., Taylor, J. R., Ferrari, R., & Joyce, T. M. (2013). Symmetric instability in the
812 gulf stream. *Deep Sea Res. Part II: Topical Studies in Oceanography*, *91*, 96–110.
- 813 Trowbridge, J., & Lentz, S. (1991). Asymmetric behavior of an oceanic boundary layer
814 above a sloping bottom. *J. Phys. Oceanogr.*, *21*(8), 1171–1185.
- 815 Umlauf, L., Smyth, W. D., & Moum, J. N. (2015). Energetics of bottom ekman layers during
816 buoyancy arrest. *J. Phys. Oceanogr.*, *45*(12), 3099–3117.
- 817 Wang, P., McWilliams, J. C., & Ménésguen, C. (2014). Ageostrophic instability in rotating,
818 stratified interior vertical shear flows. *J. Fluid Mech.*, *755*, 397–428.
- 819 Wenegrat, J. O., & Thomas, L. N. (2020). Centrifugal and symmetric instability during ek-
820 man adjustment of the bottom boundary layer. *J. Phys. Oceanogr.*, *50*(6), 1793–1812.
- 821 Wenegrat, J. O., Thomas, L. N., Gula, J., & McWilliams, J. C. (2018). Effects of the sub-
822 mesoscale on the potential vorticity budget of ocean mode waters. *J. Phys. Oceanogr.*,
823 *48*(9), 2141–2165.
- 824 Wijesekera, H., Allen, J. S., & Newberger, P. (2003). Modeling study of turbulent mixing
825 over the continental shelf: Comparison of turbulent closure schemes. *J. Geophys. Res.*
826 *: Oceans*, *108*(C3).
- 827 Wunsch, C., & Ferrari, R. (2004). Vertical mixing, energy, and the general circulation of the
828 oceans. *Annu. Rev. Fluid Mech.*, *36*, 281–314.